*Astronomy & Astrophysics* manuscript no. combine
March 1, 2013

© ESO 2013

arXiv:1203.6205v1 [astro-ph.CO] 28 Mar 2012

# Improving three-dimensional mass mapping with weak gravitational lensing through a synergy with galaxy clustering

Patrick Simon

Argelander-Institut für Astronomie, Universität Bonn, Auf dem Hügel 71, 53121 Bonn, Germany
e-mail: `psimon@astro.uni-bonn.de`

Received March 1, 2013

## ABSTRACT

*Context.* The weak gravitational lensing distortion of distant galaxy images (“sources”) probes the projected large-scale matter distribution in the Universe. The availability of redshift information in galaxy surveys also allows us to recover the radial matter distribution to a certain degree.

*Aims.* To improve the S/N in the mass mapping, we combine the lensing information with the spatial clustering of a population of galaxies that trace the matter density with a known galaxy bias.

*Methods.* We construct a minimum-variance estimator for the 3D matter density that incorporates the angular distribution of galaxy tracers, which are coarsely binned in redshift. Merely the second-order biasing of the tracers has to be known, which can in principle be self-consistently constrained in the data by lensing techniques. To study the new estimator, we generate a mock survey with galaxies that trace the matter density with a Gaussian linear stochastic bias.

*Results.* The filter smoothes and linearly mixes the individual lensing mass and tracer number density maps into a combined mass map. The weighting in the mixing depends on the S/N of the individual maps and the correlation, $R$, of the matter and galaxy density. We down-weigh the influence of the dominant tracer number density by rescaling the noise covariance in the filter. Even for a moderate mixing, the S/N in the mass map improves by a factor $\sim 2$, most strongly for $z \gtrsim 0.5$. Moreover, the systematic offset between a true and apparent mass peak distance (“$z$-shift bias”) in a lensing-only map is eliminated, even for weak correlations of $R \sim 0.4$. The mixing, however, introduces a new noise component because of the stochasticity in the matter-tracer density relation. We give a prescription of the noise level and the average radial smoothing in the Gaussian regime.

*Conclusions.* If the second-order bias of tracer galaxies can be determined from a lensing survey, the synergy technique potentially provides an option to improve the quality of a lensing 3D mass map. The detailed estimator bias and the noise, however, depends on the galaxy biasing mechanism, such that our Gaussian model may be too inaccurate at small angular scales.

**Key words.** Gravitational lensing:weak – (Cosmology:) large-scale structure – (Cosmology:) dark matter – Methods: data analysis

## 1. Introduction

The weak gravitational lensing effect is a well-established tool to infer the projected, and to some degree also deprojected, large-scale matter distribution (e.g. Tyson et al. 1990; Bonnet et al. 1994; Smail et al. 1995; Tyson & Fischer 1995; Squires et al. 1996a,b; Fischer & Tyson 1997; Clowe et al. 1998; Abdelsalam et al. 1998; Fischer 1999; Clowe et al. 2000; Umetsu & Futamase 2000; Lombardi et al. 2000; King et al. 2002; Miyazaki et al. 2002; Dahle et al. 2003; Markevitch et al. 2004; Taylor et al. 2004; Jee et al. 2005; Dietrich et al. 2005; Clowe et al. 2006; Bradač et al. 2006; Jee et al. 2007; Massey et al. 2007; Heymans et al. 2008; Bradač et al. 2008; Holhjem et al. 2009; Gavazzi et al. 2009; Okabe et al. 2010; Israel et al. 2010; Schirmer et al. 2011; Simon et al. 2012). The therein exploited coherent shear distortions of distant galaxy images (“sources”) are the result of the continuous deflection of light bundles by the intervening fluctuations in the large-scale gravitational field (e.g. Schneider 2006a,b), most prominently detectable around galaxy clusters. The lensing distortions probe the total matter content in the Universe, which makes them an excellent tool for studying the dark matter component, an essential ingredient of the standard cosmological ΛCDM model (e.g. Dodelson 2003), or for testing the dark matter hypothesis (e.g. Guzzo et al. 2008; Reyes et al. 2010), which relies too a large extend on Einstein’s general theory of relativity. Correlations between shear distortions of sources at different redshifts (cosmic shear tomography; Hu 2002) additionally constitute a promising probe for investigating the accelerated expansion of the Universe at redshifts below $z \sim 1$ (Schrabback et al. 2010).

The coherent angular shear distortion pattern can be translated into a map of projected matter fluctuations. Early non-parametric mapping algorithms, which were refined later on to obtain optimised methods for finite fields, achieved this on the basis of a catalogue of source angular positions and ellipticities only (Kaiser & Squires 1993; Broadhurst et al. 1995; Kaiser 1995; Schneider & Seitz 1995; Seitz & Schneider 1995; Schneider 1995; Seitz & Schneider 1996; Bartelmann et al. 1996; Squires & Kaiser 1996; Schneider 1996; Seitz & Schneider 1997; Seitz et al. 1998; Bridle et al. 1998; Seitz & Schneider 2001; Saini & Raychaudhury 2001; Marshall et al. 2002; Starck et al. 2006; Marshall 2006; Deb et al. 2010; Deriaz et al. 2012). With the advent of distance indicators of galaxies in wide field galaxy surveys, the purely geometric relation between shear magnitude and source (and lens) distance is incorporated into a new three-dimensional (3D) lensing algorithm to also recover information on the radial distribution of matter (Hu & Keeton 2002; Bacon & Taylor 2003; Simon et al. 2009; VanderPlas et al. 2011; Leonard et al. 2012). So far, the best studied methodologies utilise linear inversion techniques, such as Wiener filtering or a radial matter density eigenmode decomposition with a suppression of low signal-to-noise (S/N) modes. Owing to the relatively sparse and noisy sampling of the survey area with background sources, however, the resulting maps are usually very noisy, and significant detections are basically restricted to mass peaks of a galaxy cluster scale with only moderate redshift accuracy; the mass detection limit and redshift resolution declines quickly with peak distance (Simon et al. 2009, 2012). Moreover, because of the low S/N in mapping applications, the linear inversion applies a radial smoothing with a broad smoothing kernel that (a) smears out localised peaks in radial direction and (b) biases the peak distances ("$z$-shift bias"; Simon et al. 2009), which potentially renders the resulting maps hard to interpret. To attain more realistic 3D maps, the radial elongation of peaks inside the map can be mended by regularising the inversion (Leonard et al. 2012), or by finding the maximum-likelihood (ML) positions of one or a few individual mass peaks along the line-of-sight (l.o.s.) given the radial smoothing kernel and radial density profile in the map (Simon et al. 2012). But this does not alleviate the principle problem of noisy maps and inaccurate peak distances. It merely provides more realistic ML estimators for the 3D mass map. Moreover, the noise properties of the maps are likely to be complex in regularised, non-linear methods.

On the other hand, galaxy positions themselves are also tracers of the 3D matter density field and could therefore be employed to add extra information to the matter density maps that are obtained from 3D lensing. There are two complications here, however: (i) galaxies trace the matter density field only up to a systematic mismatch, which is generally dubbed "galaxy bias" (e.g. Weinberg et al. 2004), and (ii) a sampling by galaxy positions is affected by shot-noise (e.g. Martínez & Saar 2002).

Pen (2004) discussed the cross-correlation of galaxy positions, endowed with highly accurate spectroscopic redshifts, and two-dimensional (2D) lensing matter maps to improve the constraints on the matter power spectrum and facilitate the deprojection of lensing maps. The strategy of this paper is to refine the minimum-variance estimator in Simon et al. (2009) for the 3D matter density by adding the galaxy clustering information to the map making process. In contrast to Pen (2004), galaxies do not need to be equipped with accurate redshifts, however, broad redshift slices, as expected from photometric redshift surveys, suffice. Since the minimum-variance estimators (Zaroubi et al. 1995) only require $2^{\rm nd}$-order statistics of the input data to be specified, only the $2^{\rm nd}$-order bias parameters (Gaussian biasing or linear stochastic bias; Pen 1998) of the galaxy tracers have to be known. The galaxy bias as function of scale and redshift could in principle be acquired in a self-consistent approach from the data by using lensing techniques (Schneider 1998; van Waerbeke 1998; Pen et al. 2003; Fan 2003; Jullo et al. 2012; Simon 2012), or with lesser certainty from simulations (Weinberg et al. 2004), such that we henceforth assume that it is basically known. As to (ii), the galaxy sampling shot-noise is taken care of by the galaxy noise covariance within the minimum-variance estimator.

Thus, we pursue here the idea to combine 3D lensing and galaxy clustering information to map the 3D matter distribution. Towards this goal, Sect. 2 summarises the formalism of Simon et al. (2009) to obtain the matter density on a set of lens planes based upon a set of source samples binned in redshift. Furthermore, this section lays out a new formalism to obtain the galaxy number density on the lens planes for a given set of galaxy tracers, binned in redshift slices, with known linear stochastic bias. A synergy of both estimators is achieved by Sect. 3. The benefits of a synergy are explored in Sect. 4 using simulated data. Sect. 5 finishes with a summary and conclusions.

## 2. Independent reconstructions

### 2.1. Matter density on lens planes

Here, we briefly summarise the formalism already presented in Simon et al. (2009). We adopt the exact notation that is employed therein. For more details, we refer the reader to this paper.

We split the source catalogue into $i = 1\dots N_{\rm z}$ subsamples, all of which with known redshift probability distribution (p.d.f.). The complex ellipticities (Bartelmann & Schneider 2001) of the sources belonging to the $i$th subsample are binned on a 2D grid that covers the field-of-view of the survey area. This ellipticity grid is denoted by the vector $\boldsymbol{\epsilon}^{(i)}$, whose elements are the sorted pixel values of the grid. Every subsample uses the same grid geometry.

The paper assumes that the weak lensing approximation is accurate enough for the lensing catalogue on the whole, i.e., the complex ellipticities, $\boldsymbol{\epsilon}^{\rm s}$, of individual sources are unbiased estimators of the shear, $\boldsymbol{\gamma}$, for the given source redshift in the l.o.s. direction $\boldsymbol{\theta}_i$ of the source,

$$\langle\boldsymbol{\epsilon}^{\rm s}\rangle = \langle\boldsymbol{\gamma} + \epsilon^{\rm i}\rangle = \boldsymbol{\gamma}\;, \tag{1}$$

where $\epsilon^{\rm i}$ denotes the intrinsic (unlensed) complex ellipticity of a source image. Moreover, we assume a flat-sky with a Cartesian coordinate frame.

We slice the light-cone volume, for which the matter distribution is reconstructed, into $N_{\rm lp}$ slices. Within the slices, the matter density contrast is constant along the l.o.s. as approximation. The solid angle about a l.o.s. direction corresponds to one pixel of the grid. Thus, the matter density field inside a slice is fully described by the angular distribution of mean density contrasts on a plane (lens plane) and the width of the slice. The matter density contrast on a lens plane, $\boldsymbol{\delta}_{\rm m}^{(i)}$, is binned with the same grid as the source ellipticities. We represent the grids, $\boldsymbol{\epsilon}^{(i)}$ and $\boldsymbol{\delta}_{\rm m}^{(i)}$, as vectors of equally ordered pixel values. We refer to a particular pixel by $\delta_{\rm m}^{(i)}(\boldsymbol{\theta}_j)$, where $\boldsymbol{\theta}_j$ is the direction of the pixel on the sky. Therefore, our algorithm represents the 3D-matter density contrast as an approximation by a discrete set of lens planes, which numerically limits the radial resolution, and a discrete set of pixels on the sky, limiting the angular resolution.

The complete sets of ellipticity planes and lens planes are combined inside vectors of grids,

$$\boldsymbol{\epsilon} \;=\; \left[\boldsymbol{\epsilon}^{(1)},\dots,\boldsymbol{\epsilon}^{(N_{\rm z})}\right]\;, \tag{2}$$

$$\boldsymbol{\delta}_{\rm m} \;=\; \left[\boldsymbol{\delta}_{\rm m}^{(1)},\dots,\boldsymbol{\delta}_{\rm m}^{(N_{\rm lp})}\right]\;, \tag{3}$$

respectively. The brackets, grouping together the vector arguments, should be understood as big vectors that are obtained by piling up all embraced vectors on top of each other.

In the weak lensing regime, the (pixelised) lensing convergence $\kappa^{(i)}(\boldsymbol{\theta}_j)$ is, in the lowest-order Born approximation, the weighed projection of the density contrast on the lens planes:

$$\boldsymbol{\kappa} = \left[\sum_{i=1}^{N_{\rm lp}} Q_{1i}\boldsymbol{\delta}_{\rm m}^{(i)},\dots,\sum_{i=1}^{N_{\rm lp}} Q_{N_{\rm z}i}\boldsymbol{\delta}_{\rm m}^{(i)}\right] =: \mathrm{Q}\boldsymbol{\delta}_{\rm m}\;, \tag{4}$$

where the coefficients $Q_{ij}$ express the response of the $i$th convergence plane $\boldsymbol{\kappa}^{(i)}$ to the density contrast in the $j$th lens plane, namely

$$Q_{ij} = \frac{3\Omega_{\rm m}}{2D_H^2}\int_{\chi_j}^{\chi_{j+1}} {\rm d}\chi\,\frac{\overline{W}^{(i)}(\chi)\,f_{\rm K}(\chi)}{a(\chi)}\;, \tag{5}$$

where

$$\overline{W}(\chi)=\int_{\chi}^{\infty}\mathrm{d}\chi'\,\frac{f_{\rm K}(\chi'-\chi)}{f_{\rm K}(\chi')}p_{\chi}^{(i)}(\chi')\;, \tag{6}$$

$p_{\chi}^{(i)}(\chi)$ denotes the p.d.f. of sources in the $i$th source subsample, and $[\chi_j,\chi_{j+1}[$ sets the comoving radial boundaries of the $j$th matter slice. By $D_H:=c/H_0$, we mean the Hubble radius and by $f_{\rm K}(\chi)$ the (comoving) angular diameter distance. The projection from a grid vector in "$\boldsymbol{\delta}_{\rm m}$-space" to a grid vector in "$\boldsymbol{\kappa}$-space" is hence denoted by the operator $\mathsf{Q}$ that is acting on $\boldsymbol{\delta}_{\rm m}$.

The next step connects the convergence planes $\boldsymbol{\kappa}$ to the shear planes by a convolution of the lensing convergence on the grid,

$$\boldsymbol{\gamma}=\left[\mathsf{P}_{\gamma\kappa}\boldsymbol{\kappa}^{(1)},\dots,\mathsf{P}_{\gamma\kappa}\boldsymbol{\kappa}^{(N_z)}\right]=:\mathsf{P}_{\gamma\kappa}\boldsymbol{\kappa}\;, \tag{7}$$

which introduces the operator $\mathsf{P}_{\gamma\kappa}$ (Hu & Keeton 2002) to map $\boldsymbol{\kappa}^{(i)}$ to the corresponding shear plane $\boldsymbol{\gamma}^{(i)}$. In this sense, $\mathsf{P}_{\gamma\kappa}$ performs a linear transformation from $\boldsymbol{\kappa}$ to $\boldsymbol{\gamma}$-space.

Using this compact notation, we express the linear relation between the matter density (contrast) on the lens planes and the observed, binned, ellipticity planes as:

$$\boldsymbol{\epsilon}=\mathsf{P}_{\gamma\kappa}\mathsf{Q}\boldsymbol{\delta}_{\rm m}+\boldsymbol{n}_\gamma\;. \tag{8}$$

Here, an additional vector $\boldsymbol{n}_\gamma$ denotes the binned intrinsic ellipticities of the sources of all source subsamples. In the language of lensing, we consider this the noise term that dilutes the shear signal $\mathsf{P}_{\gamma\kappa}\mathsf{Q}\boldsymbol{\delta}_{\rm m}$.

For the scope of this paper, possible correlations between shear and intrinsic shapes are ignored (Hirata & Seljak 2004). A minimum-variance estimator of $\boldsymbol{\delta}_{\rm m}$ in Eq. (8) is then

$$\boldsymbol{\delta}_{\rm m,est}=\mathsf{S}_\delta\mathsf{Q}^{\rm t}\mathsf{P}^\dagger_{\gamma\kappa}\left(\mathsf{N}_\gamma^{-1}\mathsf{P}_{\gamma\kappa}\mathsf{Q}\mathsf{S}_\delta\mathsf{Q}^{\rm t}\mathsf{P}^\dagger_{\gamma\kappa}+\alpha\mathbb{1}\right)^{-1}\mathsf{N}_\gamma^{-1}\boldsymbol{\epsilon}\;. \tag{9}$$

As only input, the minimum-variance filter requires the signal covariance $\mathsf{S}_\delta=\langle\boldsymbol{\delta}_{\rm m}\boldsymbol{\delta}_{\rm m}^{\rm t}\rangle$, which specifies the presumed two-point correlation between pixel values of $\delta_{\rm m}^{(i)}(\boldsymbol{\theta})$ on the lens plane(s), and the noise covariance $\mathsf{N}_\gamma=\langle\boldsymbol{n}_\gamma\boldsymbol{n}_\gamma^{\rm t}\rangle$, which quantifies the shear pixel noise variance and the correlation of noise between different pixels. Pixels that contain no sources have infinite noise. For the prior signal covariance, correlations between pixels that belong to different lens planes are set to zero. We note here that the signal covariance does not need to be the true signal covariance in the data, although the reconstruction may be suboptimal when it is not.

The signal covariance determines the degree of smoothing in the 3D map. The smoothing is uniquely defined by the linear transformation

$$\mathsf{B}_\delta:=\left(\alpha\mathbb{1}+\mathsf{S}_\delta\mathsf{N}_\delta^{-1}\right)^{-1}\mathsf{S}_\delta\mathsf{N}_\delta^{-1}\;;\;\mathsf{N}_\delta^{-1}:=\mathsf{Q}^{\rm t}\mathsf{P}^\dagger_{\gamma\kappa}\mathsf{N}_\gamma^{-1}\mathsf{P}_{\gamma\kappa}\mathsf{Q}\;, \tag{10}$$

and can as such be utilised for a comparison of the map $\boldsymbol{\delta}_{\rm m,est}$ to a theoretical matter distribution $\boldsymbol{\delta}_{\rm m,th}$ by $\mathsf{B}_\delta\boldsymbol{\delta}_{\rm m,th}$ (Simon et al. 2012). The radial smoothing is characterised by a radial point-spread function (p.s.f.) of the filter. After smoothing with the radial p.s.f., a peak in the true matter distribution $\boldsymbol{\delta}_{\rm m,th}$ does on average not necessarily peak at the same distance as in the smoothed map, which gives rise to the so-called redshift bias or "z-bias". Inside the filter, the constant $\alpha\in[0,1]$ tunes the level of smoothing by rescaling the noise covariance.

From a practical point of view (Appendix B of Simon et al. 2009), the Wiener filter consists of a series of linear operators that is applied step-by-step from the right to left to the grids. Within this process, the signal covariance $\mathsf{S}_\delta$ is a convolution or, equivalently, a multiplication in Fourier space of Fourier modes $\tilde{f}(\boldsymbol{\ell})$ of the $i$th lens plane with the angular signal power spectrum $P_\delta^{(i)}(\ell)$, which is implicitly defined by

$$\left\langle\tilde{\delta}_{\rm m}^{(i)}(\boldsymbol{\ell})\tilde{\delta}_{\rm m}^{(i)}(\boldsymbol{\ell}')\right\rangle=(2\pi)^2\delta_{\rm D}(\boldsymbol{\ell}+\boldsymbol{\ell}')P_\delta^{(i)}(|\boldsymbol{\ell}|)\;. \tag{11}$$

We approximate the power spectrum by using Limber's equation (Kaiser 1992) in Fourier space,

$$P_\delta^{(i)}(\ell)=\frac{|\tilde{F}(\ell)|^2}{(\Delta\chi_i)^2}\int_{\chi_i}^{\chi_{i+1}}\frac{\mathrm{d}\chi}{[f_{\rm K}(\chi)]^2}P_{\rm 3d}\left(\frac{\ell}{f_{\rm K}(\chi)},\chi\right)\;, \tag{12}$$

where $\Delta\chi_i:=\chi_{i+1}-\chi_i$, $\tilde{F}(\ell)$ is the Fourier transform of the pixel window function, and $P_{\rm 3d}(k,\chi)$ is the 3D matter-density power spectrum at radial distance $\chi$ for wave-number $k$ (e.g., Smith et al. 2003), $\delta_{\rm D}(\boldsymbol{x})$ is Dirac's delta function. We denote the Fourier transforms of flat fields $f(\boldsymbol{\theta})$ on the sky by $\tilde{f}(\boldsymbol{\ell})$, defined by

$$f(\boldsymbol{\theta})=\int\frac{\mathrm{d}^2\ell}{(2\pi)^2}\,\tilde{f}(\boldsymbol{\ell})\mathrm{e}^{+\mathrm{i}\boldsymbol{\theta}\cdot\boldsymbol{\ell}}\;;\;\tilde{f}(\boldsymbol{\ell})=\int\mathrm{d}^2\theta\,f(\boldsymbol{\theta})\mathrm{e}^{-\mathrm{i}\boldsymbol{\theta}\cdot\boldsymbol{\ell}}\;. \tag{13}$$

### *2.2. Galaxy numbers densities on lens planes*

To improve the information in the 3D matter map and to possibly alleviate the $z$-shift bias, we add the information gained from galaxy positions, which also probe the matter distribution ("tracers").

In this section, however, we first visit the problem of mapping the spatial galaxy number densities. For this purpose, we estimate the number density of galaxies projected onto the previously defined lens planes. Hence, we slice the full *true* 3D galaxy distribution into $N_{\rm lp}$ distance slices with distance limits $[\chi_i,\chi_{i+1}[$. The galaxies are counted within each slice and angular grid pixel of solid angle $A_\omega$. Thereby, we receive the galaxy number density $n_{\rm g}^{(i)}(\boldsymbol{\theta}_j)=N^{(i)}(\boldsymbol{\theta}_j)/A_\omega$ in l.o.s. direction $\boldsymbol{\theta}_j$ of the $i$th slice, where $N^{(i)}(\boldsymbol{\theta}_j)$ is the number of counted galaxies. We compile the galaxy number density values inside a grid vector $\boldsymbol{n}_{\rm g}^{(i)}$, and we then arrange all grids inside a vector of grids

$$\boldsymbol{n}_{\rm g}=\left[\boldsymbol{n}_{\rm g}^{(1)},\dots,\boldsymbol{n}_{\rm g}^{(N_{\rm lp})}\right]\;. \tag{14}$$

This is the number density distribution of galaxies that the following scheme seeks to recover from a galaxy sample with inaccurate distance information. Towards this goal, we split the *observed* galaxy sample as to their redshift estimators, $z_{\rm est}\in[z(\chi_i),z(\chi_{i+1})[$, into $N_{\rm lp}$ subsamples with known radial p.d.f. $p_{\rm f}^{(i)}(\chi)$. By projecting the $i$th sample onto a 2D grid on the sky, one obtains the observed number density distribution

$$\eta_{\rm g}^{(i)}(\boldsymbol{\theta}_k)=\sum_{j=1}^{N_{\rm lp}}f_{\rm mask}(\boldsymbol{\theta}_k)p_{ij}\,n_{\rm g}^{(j)}(\boldsymbol{\theta}_k)=:\sum_{j=1}^{N_{\rm lp}}G_{ij}(\boldsymbol{\theta}_k)n_{\rm g}^{(j)}(\boldsymbol{\theta}_k)\;, \tag{15}$$

where $f_{\rm mask}\in\{0,1\}$ flags mask pixels (= 0 for mask), and

$$p_{ij}:=\int_{\chi_j}^{\chi_{j+1}}\mathrm{d}\chi\,p_{\rm f}^{(i)}(\chi) \tag{16}$$

is the probability to find a galaxy with $\chi\in[\chi_j,\chi_{j+1}[$ anywhere inside the grid $\eta_{\rm g}^{(i)}$. Owing to the redshift errors, the observed distribution on the lens planes, $\eta_{\rm g}^{(i)}(\boldsymbol{\theta}_k)$, does not exactly match the true distribution $n_{\rm g}^{(i)}(\boldsymbol{\theta}_k)$. Therefore, $0\le G_{ij}(\boldsymbol{\theta}_k)\le1$ denotes the fraction of galaxies on the $j$th lens plane that are, on average, mapped onto the grid $\eta_{\rm g}^{(i)}$. Because of masking, the total number of galaxies is not necessarily conserved, i.e., $\sum_{i=1}^{N_{\rm lp}} G_{ij}(\boldsymbol{\theta}_k)\neq 1$. By a proper arrangement of the elements $G_{ij}(\boldsymbol{\theta}_k)$ inside a matrix $\mathsf{G}$, the effect of $G_{ij}(\boldsymbol{\theta}_k)$ on the entire 3D grid $\boldsymbol{n}_{\rm g}$ can be written as

$$\boldsymbol{\eta}_{\rm g} = \mathsf{G}\boldsymbol{n}_{\rm g} + \boldsymbol{\phi}_{\rm g}\;, \tag{17}$$

where

$$\boldsymbol{\eta}_{\rm g} = \left[\boldsymbol{\eta}_{\rm g}^{(1)},\dots,\boldsymbol{\eta}_{\rm g}^{(N_{\rm lp})}\right]\;. \tag{18}$$

We presume that galaxies sample an underlying smooth galaxy number density by a discrete Poisson process (e.g., Martínez & Saar 2002). Therefore, the observable galaxy counts sample the underlying galaxy number density $\boldsymbol{n}_{\rm g}$ merely up to shot-noise, which is here formally expressed by the noise component $\boldsymbol{\phi}_{\rm g}$.

Now, by analogy with the matter density $\boldsymbol{\delta}_{\rm m}$, we can find an minimum-variance filter to estimate the true distribution of galaxies on the lens planes, namely

$$\boldsymbol{n}_{\rm g,est} = \mathsf{S}_{\rm g}\mathsf{G}^{\rm t}\left(\mathsf{N}_{\rm g}^{-1}\mathsf{G}\mathsf{S}_{\rm g}\mathsf{G}^{\rm t}+\beta\mathbb{1}\right)^{-1}\mathsf{N}_{\rm g}^{-1}\boldsymbol{\eta}_{\rm g}\;. \tag{19}$$

As before, $\mathsf{S}_{\rm g}=\langle\boldsymbol{n}_{\rm g}\boldsymbol{n}_{\rm g}^{\rm t}\rangle$ is the signal covariance, which is the angular clustering two-point correlation function of the galaxies on the lens planes, and $\mathsf{N}_{\rm g}=\langle\boldsymbol{\phi}_{\rm g}\boldsymbol{\phi}_{\rm g}^{\rm t}\rangle$ denotes the shot-noise covariance. The degree of smoothing by the Wiener filter is tunable by using $\beta\in[0,1]$, which does not need to equal the parameter $\alpha$ in Eq. (9). For the Poisson shot-noise covariance, we adopt a diagonal noise covariance, $[\mathsf{N}_{\rm g}]_{ij}=0$ for $i\neq j$, with $[\mathsf{N}_{\rm g}]_{ii}=\overline{\eta}_{\rm g}^{(k)}(\boldsymbol{\theta}_l)$ for unmasked grid pixels $\boldsymbol{\theta}_l$, and infinite noise otherwise.[1] By $\overline{\eta}_{\rm g}^{(k)}(\boldsymbol{\theta}_l)$, we denote the estimated mean number density of galaxies in pixel $\boldsymbol{\theta}_l$ of the $k$th subsample (see next section).

Like for the matter density Wiener filter, a practical implementation of the Wiener filter in Eq. (19) consists of a series of linear operations applied to $\boldsymbol{\eta}_{\rm g}$. The effect of $\mathsf{S}_{\rm g}$ is to multiply every angular mode $\tilde{f}(\boldsymbol{\ell})$ of the $i$th lens plane with the prior galaxy power spectrum $P_{\rm g}^{(i)}(\ell)$, which we define relative to the matter power spectrum using the galaxy bias factor $b^{(i)}(\ell)\geq 0$ (e.g., Tegmark & Peebles 1998),

$$\left\langle\tilde{n}_{\rm g}^{(i)}(\boldsymbol{\ell})\tilde{n}_{\rm g}^{(i)}(\boldsymbol{\ell}')\right\rangle = (2\pi)^2\delta_{\rm D}(\boldsymbol{\ell}+\boldsymbol{\ell}')\,\underbrace{\left[\overline{n}_{\rm g}^{(i)}b^{(i)}(|\boldsymbol{\ell}|)\right]^2P_\delta^{(i)}(|\boldsymbol{\ell}|)}_{P_{\rm g}^{(i)}(\ell)}\;, \tag{20}$$

where $\overline{n}_{\rm g}^{(i)}$ denotes the true mean number density of galaxies on the $i$th lens plane. For this definition of the bias factor, the shot-noise contribution to the galaxy power spectrum is excluded as it is already accounted for in $\boldsymbol{\phi}_{\rm g}$.

The angular bias factor $b^{(i)}(\ell)$ is related to the 3D bias factor $b(k,\chi)$, where $k$ is the comoving 3D wave-number, by a projection that is approximated by Limber's equation,

$$\begin{aligned}&[b^{(i)}(\ell)]^2P_\delta^{(i)}(\ell)\\&\quad=\frac{|\tilde{F}(\ell)|^2}{[\Delta\chi_i]^2}\int_{\chi_i}^{\chi_{i+1}}\frac{{\rm d}\chi}{[f_{\rm K}(\chi)]^2}\,b^2\left(\frac{\ell}{f_{\rm K}(\chi)},\chi\right)P_{\rm 3d}\left(\frac{\ell}{f_{\rm K}(\chi)},\chi\right)\;;\end{aligned} \tag{21}$$

$P_\delta^{(i)}(\ell)$ is given by Eq. (12). For this approximation, we assume that the number density of galaxies stays constant inside the slice.

### 2.3. True mean galaxy numbers

The true galaxy number densities $\overline{n}_{\rm g}^{(i)}$ in Eq. (20) have to be derived from the data itself. For an estimator of $\overline{n}_{\rm g}^{(i)}$, we go back to Eq. (17), which relates the observed number of galaxies, $\boldsymbol{\eta}_{\rm g}$, to the true number on the lens planes, $\boldsymbol{n}_{\rm g}$. For an statistical ensemble average of this relation, we expect

$$\overline{\boldsymbol{\eta}}_{\rm g} := \left\langle\boldsymbol{\eta}_{\rm g}\right\rangle = \mathsf{G}\overline{\boldsymbol{n}}_{\rm g}\;, \tag{22}$$

wherein, however, all elements $\overline{n}_{\rm g}^{(i)}(\boldsymbol{\theta}_j)$ equal one number $\overline{n}_{\rm g}^{(i)}$ owing to the statistical homogeneity of the galaxy number density fields, hence

$$\overline{\eta}_{\rm g}^{(i)}(\boldsymbol{\theta}_k) = \sum_{j=1}^{N_{\rm lp}}\mathsf{G}_{ij}(\boldsymbol{\theta}_k)\,\overline{n}_{\rm g}^{(j)}\;. \tag{23}$$

Summing over all pixels, $N_{\rm p}$ in total, of the $i$th tracer sample yields

$$\overline{\mathcal{X}}_{\rm g}^{(i)} := \frac{1}{N_{\rm p}}\sum_{k=1}^{N_{\rm p}}\overline{\eta}_{\rm g}^{(i)}(\boldsymbol{\theta}_k) = \sum_{j=1}^{N_{\rm lp}}\overline{\mathsf{G}}_{ij}\,\overline{n}_{\rm g}^{(j)}\;, \tag{24}$$

where

$$\overline{\mathsf{G}}_{ij} := N_{\rm p}^{-1}\sum_{k=1}^{N_{\rm p}}G_{ij}(\boldsymbol{\theta}_k) \tag{25}$$

averages $\mathsf{G}_{ij}$ over the area of the grid. Inverting the former equation, gives

$$\overline{n}_{\rm g}^{(i)} = \sum_{j=1}^{N_{\rm lp}}\left[\overline{\mathsf{G}}^{-1}\right]_{ij}\overline{\mathcal{X}}_{\rm g}^{(j)}\;\;;\;\;\overline{\mathcal{X}}_{\rm g}^{(i)}\approx\frac{1}{N_{\rm p}}\sum_{k=1}^{N_{\rm p}}\eta_{\rm g}^{(i)}(\boldsymbol{\theta}_k)\;. \tag{26}$$

For an unbiased estimator of $\overline{\mathcal{X}}_{\rm g}^{(i)}$ on the r.h.s., we insert the observed galaxy number densities, i.e., $\overline{\eta}_{\rm g}^{(i)}(\boldsymbol{\theta}_k)=\eta_{\rm g}^{(i)}(\boldsymbol{\theta}_k)$. The value of $\overline{\eta}_{\rm g}^{(i)}(\boldsymbol{\theta}_k)$, which is utilised for the noise covariance $\mathsf{N}_{\rm g}$ in the foregoing section, is computed from Eq. (23) and the estimated $\overline{n}_{\rm g}^{(i)}$.

In the simple case of negligible redshift errors, we find $\mathsf{G}_{ij}(\boldsymbol{\theta}_k)=\delta_{ij}^{\rm K}f_{\rm mask}(\boldsymbol{\theta}_k)$, where $\delta_{ij}^{\rm K}$ denotes the Kronecker symbol. In this case, we consequently find

$$[\overline{\mathsf{G}}^{-1}]_{ij} = \delta_{ij}^{\rm K}\frac{N_{\rm p}}{N}\;, \tag{27}$$

for $N$ being the number of unmasked pixels. Moreover, we find $\overline{n}_{\rm g}^{(i)}=N_{\rm p}N_{\rm g}^{(i)}/(N\Omega)$ for a number $N_{\rm g}^{(i)}$ of galaxies within the $i$th subsample and a survey area $\Omega$. Thus, the galaxy number density $N_{\rm g}^{(i)}/\Omega$ is scaled up by $N_{\rm p}/N$ to account for the mask.

However, the estimator in Eq. (26) has one caveat since $\overline{\eta}_{\rm g}^{(i)}$ are basically a convolution of $\overline{n}_{\rm g}^{(i)}$ with the redshift error of galaxies. A deconvolution through $\overline{\mathsf{G}}^{-1}$ possibly results in oscillating and negative values for $\overline{n}_{\rm g}^{(i)}$. We therefore regularise Eq. (26) by a constrained deconvolution $\overline{n}_{\rm g}^{(i)}$ that maximises the likelihood

$$\ln\mathcal{L}(\overline{\boldsymbol{n}}_{\rm g}|\overline{\boldsymbol{\eta}}_{\rm g}) = \left(\overline{\mathsf{G}}\overline{\boldsymbol{n}}_{\rm g}-\overline{\boldsymbol{\eta}}_{\rm g}\right)^{\rm t}\mathsf{N}_\eta^{-1}\left(\overline{\mathsf{G}}\overline{\boldsymbol{n}}_{\rm g}-\overline{\boldsymbol{\eta}}_{\rm g}\right) \tag{28}$$

under the condition that $\overline{n}_{\rm g}^{(i)}\geq 0$ for all $i$. We determine this solution numerically. The additional covariance $\mathsf{N}_\eta$ can be used to give different weights to the observed $\overline{\eta}_{\rm g}^{(i)}$ values, for example by weighing with the number of galaxies in each galaxy sample in order to account for the galaxy shot-noise. For equal weights, we simply set $\mathsf{N}_\eta=\mathbb{1}$.

---

[1] The Wiener filter in the given form requires the inverse noise covariance, such that elements with infinite noise on the diagonal are zero.

## 3. Combined reconstruction

### 3.1. Minimum-variance estimator

Up to here, we have considered the galaxy number density and matter density fields separately. However, $\boldsymbol{\eta}_{\rm g}$ contains information about $\boldsymbol{\delta}_{\rm m}$ and vice versa, as galaxies trace the matter distribution to a certain degree. On a statistical level, this relation is reflected by a non-vanishing cross-correlation

$$\mathsf{S}_{\delta{\rm g}} = \langle \boldsymbol{\delta}_{\rm m} \boldsymbol{n}_{\rm g}^{\rm t} \rangle \tag{29}$$

for pairs of pixels on the same lens plane, which has not entered our formalism so far. Slices are thought to be wide enough, such that correlations between pixels belonging to different lens plane are negligible.

We combine the $\boldsymbol{\delta}_{\rm m}$- and $\boldsymbol{n}_{\rm g}$-grids inside one new vector

$$\boldsymbol{s} := \left[\boldsymbol{\delta}_{\rm m}, \boldsymbol{n}_{\rm g}\right] \;, \tag{30}$$

which relates to the observed shear and tracer number density grids,

$$\boldsymbol{d} := \left[\boldsymbol{\gamma}, \boldsymbol{\eta}_{\rm g}\right] \;, \tag{31}$$

according to the Eqs. (8) and (17) via

$$\boldsymbol{d} = \left[\mathsf{P}_{\gamma\kappa}\mathsf{Q}\boldsymbol{\delta}_{\rm m}, \mathsf{G}\boldsymbol{n}_{\rm g}\right] + \boldsymbol{n} =: \mathsf{R}\boldsymbol{s} + \boldsymbol{n} \,, \tag{32}$$

where the combined noise vector is

$$\boldsymbol{n} := \left[\boldsymbol{n}_{\gamma}, \boldsymbol{\phi}_{\rm g}\right] \;. \tag{33}$$

In this compact notation, the action of a matrix

$$\mathsf{A} = \begin{pmatrix} \mathsf{A}_{11} & \mathsf{A}_{12} \\ \mathsf{A}_{21} & \mathsf{A}_{22} \end{pmatrix} \tag{34}$$

on a product vector $\boldsymbol{v} = [\boldsymbol{v}_1, \boldsymbol{v}_2]$ is defined as

$$\mathsf{A}\boldsymbol{v} := \left[\mathsf{A}_{11}\boldsymbol{v}_1 + \mathsf{A}_{12}\boldsymbol{v}_2, \mathsf{A}_{21}\boldsymbol{v}_1 + \mathsf{A}_{22}\boldsymbol{v}_2\right] . \tag{35}$$

In this sense, the projection matrix $\mathsf{R}$ is

$$\mathsf{R} = \begin{pmatrix} \mathsf{P}_{\gamma\kappa}\mathsf{Q} & 0 \\ 0 & \mathsf{G} \end{pmatrix} . \tag{36}$$

Following the usual assumptions of a minimum-variance filter, the optimal filter for estimating $\boldsymbol{s}$ from $\boldsymbol{d}$ in this combined problem is

$$\boldsymbol{s}_{\rm est} = \mathsf{S}\mathsf{R}^\dagger\left(\mathsf{N}_{\alpha\beta}^{-1}\mathsf{R}\mathsf{S}\mathsf{R}^\dagger + 1\right)^{-1}\mathsf{N}_{\alpha\beta}^{-1}\,\boldsymbol{d} \,, \tag{37}$$

which uses as short-hand notations

$$\mathsf{S} = \begin{pmatrix} \mathsf{S}_{\delta} & \mathsf{S}_{\delta{\rm g}} \\ \mathsf{S}_{\delta{\rm g}}^{\rm t} & \mathsf{S}_{\rm g} \end{pmatrix} ;\; \mathsf{N}_{\alpha\beta} = \begin{pmatrix} \alpha\mathsf{N}_{\gamma} & 0 \\ 0 & \beta\mathsf{N}_{\rm g} \end{pmatrix} ;\; \mathsf{R}^\dagger = \begin{pmatrix} \mathsf{Q}^{\rm t}\mathsf{P}_{\gamma\kappa}^\dagger & 0 \\ 0 & \mathsf{G}^{\rm t} \end{pmatrix} . \tag{38}$$

The galaxy shot-noise $\boldsymbol{\phi}_{\rm g}$ and the intrinsic ellipticities of the sources, which are comprised in $\boldsymbol{n}_{\gamma}$, are assumed to be uncorrelated. By choosing different tuning parameters $\alpha \neq \beta$, the impact of the Wiener smoothing can be adjusted independently for the matter and galaxy map.

The novelty of the combined reconstruction is that tracer number and matter density maps will exchange information, if the cross-correlation matrix $\mathsf{S}_{\delta{\rm g}}$ is non-vanishing. In a practical implementation of the filter (37), we apply, as before, step by step linear operations to the grids stored inside $\boldsymbol{d}$. As with the previous operators $\mathsf{S}_{\delta}$ and $\mathsf{S}_{\rm g}$, the application of $\mathsf{S}_{\delta{\rm g}}$ amounts to a multiplication of angular grid modes with the cross-correlation power spectrum $P_{\delta{\rm g}}^{(i)}(\ell)$, determined by

$$\left\langle \tilde{n}_{\rm g}^{(i)}(\boldsymbol{\ell})\tilde{\delta}_{\rm m}^{(i)}(\boldsymbol{\ell}')\right\rangle = (2\pi)^2\delta_{\rm D}(\boldsymbol{\ell}+\boldsymbol{\ell}')\; \underbrace{\overline{n}_{\rm g}^{(i)} r^{(i)}(|\boldsymbol{\ell}|) b^{(i)}(|\boldsymbol{\ell}|) P_{\delta}^{(i)}(|\boldsymbol{\ell}|)}_{=P_{\delta{\rm g}}(\ell)} \;. \tag{39}$$

We define $P_{\delta{\rm g}}^{(i)}(\ell)$ with respect to the matter power spectrum $P_{\delta}^{(i)}(\ell)$ by employing the galaxy-matter cross-correlation factor $r^{(i)}(\ell)$ (Tegmark & Peebles 1998). The angular function $r^{(i)}(\ell)$ is approximately related to the 3D correlation factor $r(k,\chi)$ according to

$$\begin{aligned} & r^{(i)}(\ell)b^{(i)}(\ell)P_{\delta}^{(i)}(\ell) \\ & \quad = \frac{|\tilde{F}(\ell)|^2}{[\Delta\chi_i]^2}\int_{\chi_i}^{\chi_{i+1}}\frac{{\rm d}\chi}{[f_{\rm K}(\chi)]^2}\, r\left(k_\ell,\chi\right) b\left(k_\ell,\chi\right) P_{\rm 3d}\left(k_\ell,\chi\right) \;, \end{aligned} \tag{40}$$

where $k_\ell := \ell/f_{\rm K}(\chi)$.

To understand the mode of operation of the minimum-variance filter in Eq. (37), it is instructive to recast it into the mathematically equivalent form

$$\boldsymbol{s}_{\rm est} = \underbrace{\left(1 + \mathsf{S}\mathsf{N}_{\delta n_{\rm g}}^{-1}\right)^{-1}\mathsf{S}\mathsf{N}_{\delta n_{\rm g}}^{-1}}_{\rm Step-2} \times \underbrace{\mathsf{N}_{\delta n_{\rm g}}\mathsf{R}^\dagger\mathsf{N}^{-1}}_{\rm Step-1}\;\boldsymbol{d} \;, \tag{41}$$

where $\mathsf{N}_{\delta n_{\rm g}}^{-1} := \mathsf{R}^\dagger\mathsf{N}_{\alpha\beta}^{-1}\mathsf{R}$ denotes the inverse noise covariance of the matter and tracer density maps after the application of the unbiased estimator in Step-1.[2] Step-1 involves no Wiener smoothing, hence matrix $\mathsf{S}$, to construct the maps. As this is usually too noisy, we apply an additional smoothing to these maps by virtue of the Wiener filter in Step-2. This filter linearly combines, averages pixel values in the maps based upon the expected S/N in the unbiased maps. It is this Step-2, the analogue of the matrix $\mathsf{B}_{\delta}$ in Sect. 2.1, that introduces biases into the maps, especially through a radial smoothing. Moreover, only Step-2 formally mixes pixels from the mass map and the tracer number density map by means of the off-diagonal matrix $\mathsf{S}_{\delta{\rm g}}$. Therefore, Step-1 makes independent mass and tracer maps that are only later on combined in Step-2 according to our prior knowledge of the correlation of both. Setting $\alpha = \beta = 0$ results in a unity matrix for Step-2, i.e., no smoothing.

### 3.2. Fourier space representation

For shear and galaxy number noise homogeneous over infinite grids with no gaps, the estimator in Eq. (37) takes a simple form in Fourier space. Under this idealistic conditions, the angular modes

$$\tilde{\boldsymbol{s}}(\boldsymbol{\ell}) = \left[\tilde{\boldsymbol{\delta}}_{\rm m}(\boldsymbol{\ell}), \tilde{\boldsymbol{n}}_{\rm g}(\boldsymbol{\ell})\right] \tag{42}$$

are only linear functions of the $\eta_{\rm g}$- and $\gamma$-modes of the same $\boldsymbol{\ell}$; there is no mixing between modes of different $\ell$. Therefore, a reconstruction is then done most easily in Fourier space by

$$\widetilde{\boldsymbol{s}}_{\rm est}(\boldsymbol{\ell}) = \widetilde{\mathsf{S}}_\ell\widetilde{\mathsf{R}}_\ell^\dagger\left(\widetilde{\mathsf{R}}_\ell\widetilde{\mathsf{S}}_\ell\widetilde{\mathsf{R}}_\ell^\dagger + \widetilde{\mathsf{N}}_{\alpha\beta}\right)^{-1}\widetilde{\boldsymbol{d}}(\boldsymbol{\ell}) \;, \tag{43}$$

---

[2] Our implementation of the estimator explicitly assumes that both the matter and the tracer density contrast vanish when averaged over each lens plane to lift the mass-sheet degeneracy.

where $\widetilde{\boldsymbol{d}}(\boldsymbol{\ell})=\left[\widetilde{\boldsymbol{\gamma}}(\boldsymbol{\ell}),\widetilde{\boldsymbol{\eta}}_{\rm g}(\boldsymbol{\ell})\right]$ are the observable input grids. The covariance matrix of the (homogeneous) noise is

$$\widetilde{\mathsf{N}}_{\alpha\beta}=\mathrm{diag}\left\{\frac{\alpha\sigma_\epsilon^2}{\overline{n}_{\rm s}^{(1)}},\ldots,\frac{\alpha\sigma_\epsilon^2}{\overline{n}_{\rm s}^{(N_z)}},\beta\overline{\eta}_{\rm g}^{(1)},\ldots,\beta\overline{\eta}_{\rm g}^{(N_{\rm lp})}\right\}\,, \tag{44}$$

where $\overline{n}_{\rm s}^{(i)}$ is the mean *source* number density of the $i$th source sample (out of in total $N_z$), $\sigma_\epsilon^2=\langle\epsilon^{\rm i}[\epsilon^{\rm i}]^*\rangle$ is their intrinsic shape noise variance, and $\overline{\eta}_{\rm g}^{(i)}$ is the Poisson shot-noise power (white noise). Possible noise contributions owing to intrinsic alignments of sources are ignored here, hence $\widetilde{\mathsf{N}}_{\alpha\beta}$ has no off-diagonal elements. Furthermore, one has[3]

$$\widetilde{\mathsf{R}}_\ell=\begin{pmatrix}D(\boldsymbol{\ell})\mathsf{Q} & 0\\ 0 & \mathsf{G}\end{pmatrix}\;;\;\widetilde{\mathsf{R}}_\ell^\dagger=\begin{pmatrix}D^*(\boldsymbol{\ell})\mathsf{Q}^{\rm t} & 0\\ 0 & \mathsf{G}^{\rm t}\end{pmatrix}\,, \tag{45}$$

where $D(\boldsymbol{\ell})=\boldsymbol{\ell}/\boldsymbol{\ell}^*$ (Kaiser & Squires 1993); for $\boldsymbol{\ell}=0$, we set $D(\boldsymbol{\ell})=0$. The signal covariance is

$$\widetilde{\mathsf{S}}_\ell=\begin{pmatrix}\widetilde{\mathsf{S}}_\delta(\ell) & \widetilde{\mathsf{S}}_{\delta{\rm g}}(\ell)\\ \widetilde{\mathsf{S}}_{\delta{\rm g}}(\ell) & \widetilde{\mathsf{S}}_{\rm g}(\ell)\end{pmatrix} \tag{46}$$

with

$$\widetilde{\mathsf{S}}_\delta(\ell)\;=\;\mathrm{diag}\left\{P_\delta^{(1)}(\ell),\ldots,P_\delta^{(i)}(\ell),\ldots,P_\delta^{(N_{\rm lp})}(\ell)\right\}\,, \tag{47}$$

$$\widetilde{\mathsf{S}}_{\delta{\rm g}}(\ell)\;=\;\mathrm{diag}\left\{\ldots,\overline{n}_{\rm g}^{(i)}r^{(i)}(\ell)b^{(i)}(\ell)P_\delta^{(i)}(\ell),\ldots\right\}\,, \tag{48}$$

$$\widetilde{\mathsf{S}}_{\rm g}(\ell)\;=\;\mathrm{diag}\left\{\ldots,[\overline{n}_{\rm g}^{(i)}b^{(i)}(\ell)]^2P_\delta^{(i)}(\ell),\ldots\right\}\,. \tag{49}$$

Because of the diagonal structure of the last three matrices, the matrix $\widetilde{\mathsf{S}}_\ell$ acting on a vector $\widetilde{\boldsymbol{v}}(\boldsymbol{\ell})$ actually only mixes the matter and tracer density modes from the same lens plane. Thus, rearranging the grids inside $\widetilde{\boldsymbol{v}}(\boldsymbol{\ell})$, and pairing together matter and tracer density modes of the same lens plane, renders $\widetilde{\mathsf{S}}_{\boldsymbol{\ell}}$ a diagonal block matrix

$$\widetilde{\mathsf{S}}_\ell=\mathrm{diag}\left\{\widetilde{\mathsf{S}}_\ell^{(1)},\ldots,\widetilde{\mathsf{S}}_\ell^{(N_{\rm lp})}\right\} \tag{50}$$

with the $2\times2$-blocks

$$\widetilde{\mathsf{S}}_\ell^{(i)}=\begin{pmatrix}1 & \overline{n}_{\rm g}^{(i)}r^{(i)}(\ell)b^{(i)}(\ell)\\ \overline{n}_{\rm g}^{(i)}r^{(i)}(\ell)b^{(i)}(\ell) & [\overline{n}_{\rm g}^{(i)}b^{(i)}(\ell)]^2\end{pmatrix}\times P_\delta^{(i)}(\ell) \tag{51}$$

on the diagonal. This structure is useful when implementing the estimator in practise. Clearly, modes will not affect each other when $r^{(i)}(\ell)=0$ with no improvement by a synergy of lensing and galaxy tracers.

## 4. Mock survey study

We move on to quantify the impact of a joint reconstruction by considering an idealised survey with homogeneous noise and a $\mathsf{G}$ that is independent of the pixel position. As a fiducial cosmology, this paper uses a standard flat $\Lambda$CDM model with matter density parameter $\Omega_{\rm m}=0.27$, of which baryons are $\Omega_{\rm b}=0.046$, and a Hubble parameter $H_0=h\,100\,{\rm km\,s^{-1}\,Mpc^{-1}}$ with $h=0.704$. The normalisation of the matter fluctuations within a sphere of radius $8\,h^{-1}{\rm Mpc}$ at redshift zero is $\sigma_8=0.81$. For the spectral index of the primordial matter power spectrum, we use $n_{\rm s}=0.96$.

### 4.1. Fiducial survey parameters

For the fiducial survey, we split the source galaxy catalogue into $N_z=20$ equally sized redshift slices of width $\Delta z=0.1$, spanning the redshift range $z=0\ldots2.0$. For the sources, we neglect the effect of redshift errors greater than the width of the redshift slices, such that the true p.d.f. $p_z^{(i)}(z)$ of sources of the $i$th slice is well-described within $z\in[z_i,z_{i+1}]$ by the p.d.f. of redshift estimates of the full sample,

$$p_z(z)\propto z^2\exp\left(-\left(\frac{z}{z_0}\right)^\lambda\right)\,, \tag{52}$$

where $z_0=0.57$, $\lambda=1.5$, and $z_i=(i-1)\Delta z$. We represent the reconstruction volume by $N_{\rm lp}=10$ lens planes between $z=0$ and $z=2$, centred within slices of moderate width $\Delta z_{\rm lp}=0.2$. The total number density of sources on the sky is $\overline{n}=30\,{\rm arcmin}^{-2}$ with an intrinsic shape noise of $\sigma_\epsilon=0.3$.

To support the matter density reconstruction, we include fiducial galaxy tracers with known galaxy bias. For simplicity, their p.d.f. of redshift estimates is identical to $p_z(z)$. Contrary to the sources, however, we now also emulate the effect of redshift errors by adopting a root-mean-square (r.m.s.) accuracy of $\sigma_z(z)=0.04(1+z)$ (Gaussian errors), which is built into $\mathsf{G}$ in Eq. (15). The slicing scheme for the tracers is equivalent to the scheme of the sources. From this, we compute the average number density of tracers $\overline{n}_{\rm g}^{(i)}$ and $\overline{\eta}_{\rm g}^{(i)}$ from Eq. (23) for each redshift slice, and the true redshift distributions $p_{\rm f}^{(i)}(z)$ by piecewise convolving the p.d.f. $p_z(z)$ with a Gaussian kernel of r.m.s. $\sigma_z(z)$. For low redshifts, we have $\overline{\eta}_{\rm g}^{(i)}\approx\overline{n}_{\rm g}^{(i)}$, but we find differences at higher redshifts where $\Delta z_{\rm lp}\approx\sigma_z$. For the fiducial survey, we reduce the total number of tracers to 10 percent of the sources, $\overline{n}_{\rm g}=3\,{\rm arcmin}^{-2}$, since a reconstruction realistically requires a specifically selected tracer population for an accurately known bias. Here, the tracers are clustered as the matter, $b(\ell)=1$ for all redshifts, but, more relevantly, we assume a slight stochasticity on all scales, namely $r(\ell)=0.8$. A high correlation, $r\gtrsim0.5$, for various galaxy populations is expected from theoretical models (e.g., Guzik & Seljak 2001) and observed for some cases (Hoekstra et al. 2002; Simon et al. 2007; Jullo et al. 2012). As model for the cosmic average 3D matter power spectrum $P_{\rm 3d}(k,\chi)$, we devise the prescription by Smith et al. (2003), which is used for the signal matrix $\widetilde{\mathsf{S}}_\ell$.

### 4.2. Signal-to-noise improvement

With the estimator (43) at hand, we forecast the S/N of the matter and tracer number density modes as function of angular wavenumber $\ell$. To this end, we compare, by analogy to Simon et al. (2009), the *cosmic average* power spectrum of the reconstructed matter and galaxy number density modes on the lens planes,

$$\mathsf{P}_{\rm s}(\ell):=\widetilde{\mathsf{W}}_\ell\widetilde{\mathsf{S}}_\ell\widetilde{\mathsf{W}}_\ell^\dagger\,, \tag{53}$$

to the predicted noise in their reconstruction,

$$\mathsf{P}_{\rm n}(\ell):=\widetilde{\mathsf{W}}_\ell\widetilde{\mathsf{X}}_\ell\widetilde{\mathsf{W}}_\ell^\dagger\,, \tag{54}$$

where we use

$$\widetilde{\mathsf{X}}_\ell:=\left(\widetilde{\mathsf{R}}_\ell^\dagger\widetilde{\mathsf{N}}_{\alpha\beta}^{-1}\widetilde{\mathsf{R}}_\ell\right)^{-1}\;;\;\widetilde{\mathsf{W}}_\ell:=\widetilde{\mathsf{S}}_\ell\left(\widetilde{\mathsf{S}}_\ell+\widetilde{\mathsf{X}}_\ell\right)^{-1}\,. \tag{55}$$

In this setup, the Wiener filter $\widetilde{\mathsf{W}}_\ell$ devises the actual signal power $\widetilde{\mathsf{S}}_\ell$ present in the data. As pointed out earlier, this is not a necessity, but is required for an optimal minimum-variance filter.

---

[3] Here, $\mathsf{G}$ does not depend on $\boldsymbol{\theta}_k$.

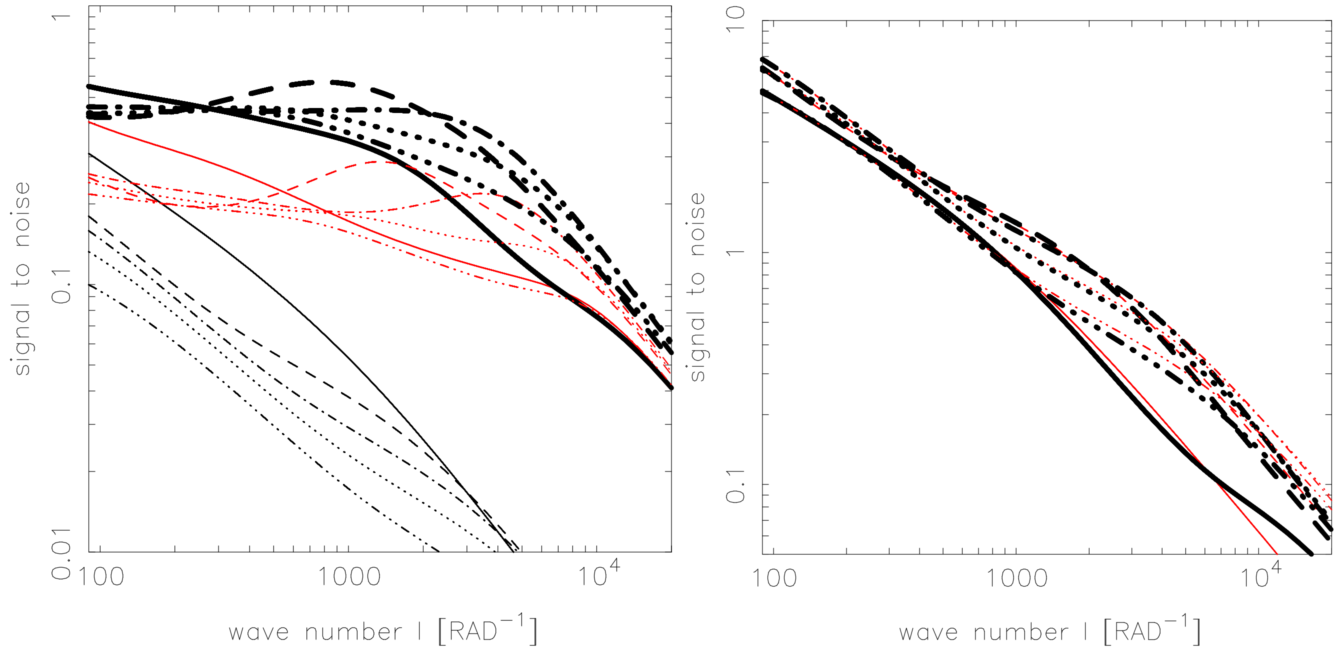

**Fig. 1.** S/N of density modes for the matter density maps (left panel) and galaxy tracer density maps (right panel). The lines assume cosmic-average fluctuations in the density fields and $b(\ell) = 1$ for the tracers. Different lines styles correspond to different lens plane redshifts: $z = 0.1$ (solid), $z = 0.3$ (dashed), $z = 0.5$ (dashed-dotted), $z = 0.7$ (dotted), $z = 0.9$ (dashed-dotted-dotted). The black thin lines do not employ any smoothing, while red thins lines use smoothing; both use no mixing of lensing and galaxy clustering information. In the right panel, red and black thin lines coincide. Thick lines depict values in a Wiener smoothed map ($\alpha = 0.01$, $\beta = 0.1$) and a mixing with $r(\ell) = 0.8$ for all redshifts.

For $\alpha = \beta = 0$ (no smoothing), the noise covariance is $\mathsf{P}_{\rm n}(\ell) = \widetilde{\mathsf{X}}_\ell$. For the following, we set $\alpha = 0.01$ to be consistent with Fig. 11 of Simon et al. (2009) for a lensing-only reconstruction with a transverse filter. The parameter $\alpha$ must not be too close to unity, as this results in a too much radial smoothing, which moves basically all mass peaks to the middle of the reconstruction volume (no radial information). In order to give the tracers not too much weight in the joint reconstruction, we set $\beta = 0.1$. A parameter $\beta$ smaller than $\alpha$ is a means to downweigh the impact of the tracers in the joint reconstruction. By our choice of parameters, the Wiener filter assumes that the galaxy shot-noise is larger by a factor of $\sqrt{\beta/\alpha} \approx 3.2$ with respect to the shape noise, thereby giving less weight to the galaxy clustering information. In addition, $\alpha = 0.01$ utilises a Wiener filter that assumes shape noise smaller by a factor of $\sqrt{\alpha} = 0.1$ than in the data and thus applies less smoothing to the maps. Our goal is to aid the 3D mass mapping a little by adding some galaxy tracer information, rather than being completely dominated by the tracers, which usually probe the matter density with considerably larger S/N compared to lensing – at least, if the galaxy bias is known; compare the thin black lines in the left to the red lines in the right panel of Fig. 1.

Fig. 1 depicts the S/N of the lens plane density modes as function of angular scale and lens plane redshift. In the left panel, we have the matter density modes, in the right panel the tracer number density modes. Different line styles correspond to different lens planes, the thin lines to reconstructions with mode mixing switched off, i.e., $r(\ell) = 0$, and the thick lines to the joint reconstruction. Clearly, as discussed in length in the recent literature (Hu & Keeton 2002; Simon et al. 2009; VanderPlas et al. 2011), a lensing-only map absolutely requires some radial smoothing, which is seen here by comparing the low S/N of the thin black lines to the boosted S/N in the red lines. Adding mode mixing with $r(\ell) = 0.8$ and the previous tuning parameters, further boosts the S/N in the mass map; here by a moderate factor of about two (red lines vs. thick black lines). An exception are angular scales of roughly one arcmin or smaller, where the shot-noise of the tracers starts to dominate their clustering signal.

The impact of mixing on the S/N of the tracer number density maps (right panel) is small, most prominently on the small angular scales. This changes slightly, if we choose an even larger tuning parameter $\beta$ (not shown): a larger $\beta$ scales up the shot-noise matrix of the tracers inside the Wiener filter, attributing even more weight to the lensing data in the joint reconstruction. As the S/N of the tracers in the data is actually higher than that of the shear, this will result in a *decreased* S/N for the galaxy number density maps in comparison to a reconstruction with no mixing; the joint reconstruction is not optimal as to the map noise.

We also observe here that for a cosmic average power in the density fields, the reconstruction algorithm recovers the density modes only with a poor $\mathrm{S/N} < 1$ on sub-degree scales for the fiducial survey. This reiterates the past observations that mapping with lensing, or in a combined reconstruction still dominated by lensing, may only be feasible for mass peaks largely exceeding the cosmic average power spectrum, such as galaxy clusters.

### 4.3. Radial point spread function

We now explore the impact on the radial p.s.f. in the matter maps by mixing 3D lensing information with the number densities of tracers. The radial p.s.f. is the average sight-line profile in the smoothed matter map of a single mass peak that is situated at a lens plane in the un-smoothed matter field. Ideally, the p.s.f. spikes at the true mass peak redshift (no $z$-shift bias). We assume a homogeneous survey, such that the choice of the l.o.s. direction $\boldsymbol{\theta}$ is irrelevant. We hence arbitrarily pick $\boldsymbol{\theta} = 0$ as reference direction and omit the pixel index $\boldsymbol{\theta}$ in the following.

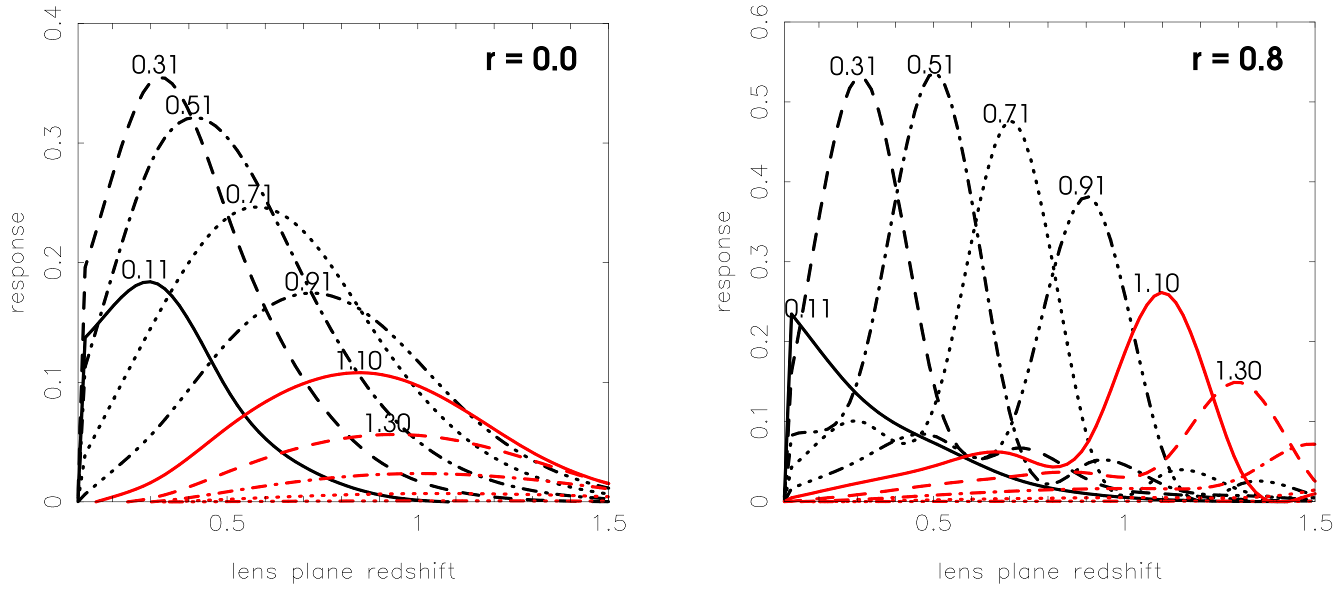

**Fig. 2.** The radial p.s.f. in the smoothed mass maps for the case $r(\ell) = 0.8$ (right panel) and no mixing of lensing and galaxy clustering ($r(\ell) = 0$; left panel). The details of the fiducial survey are found in Sect. 4.1. Both panels adopt $\alpha = 0.01$ and $\beta = 0.1$. The redshifts of the density peaks in the un-smoothed maps are the small number labels, which are only shown up to $z = 1.3$. The map pixel size is $\Theta_s = 1$ arcmin.

We consider a singular test density peak with profile $\delta_m(\chi) = A_p\delta_D(\chi - \bar{\chi}_i)$ in the un-smoothed map. It is located at the distance $\bar{\chi}_i := (\chi_i + \chi_{i+1})/2$ of the $i$th lens plane. For circular pixels with angular radius $\Theta_s$, the pixel value of this peak is in the un-smoothed map

$$F(\boldsymbol{\Delta\theta}) = \begin{cases} A_p(\pi\Theta_s^2)^{-1} & \text{for } |\boldsymbol{\Delta\theta}| \le \Theta_s \\ 0 & \text{otherwise} \end{cases} , \tag{56}$$

or in Fourier space

$$\widetilde{F}(\ell\Theta_s) = \frac{2A_p J_1(\ell\Theta_s)}{\ell\Theta_s} . \tag{57}$$

Because of the linearity of the reconstruction algorithm, the peak amplitude is unimportant for the shape of the radial p.s.f. We therefore simply set $A_p = 1$ henceforth. Unlike the discussion in Simon et al. (2009) for calculating the radial p.s.f., we here have also to factor in the tracer number density on the $i$th lens plane (and same direction $\boldsymbol{\theta}$). As this is a random variable for $r(\ell) \neq 1$, we define the p.s.f. as the radial density profile in the smoothed map given a matter peak $\tilde{\delta}_m^{(i)}(\ell) = \widetilde{F}(\Theta_s\ell)$ on the $i$th lens plane marginalised over the tracer density $\tilde{n}_g^{(i)}(\ell)$, which is associated with the mass peak. This conditional mean tracer number density is given by

$$\tilde{n}_g^{(i)}(\ell; F) := \left\langle \tilde{n}_g^{(i)}(\ell) \middle| \tilde{\delta}_m^{(i)}(\ell) \right\rangle_n \approx \bar{n}_g^{(i)} \widetilde{F}(\Theta_s\ell) r^{(i)}(\ell) b^{(i)}(\ell) , \tag{58}$$

where the conditional ensemble average

$$\langle x|y\rangle_n = \frac{\int \mathrm{d}x\, P(x,y)x}{\int \mathrm{d}x\, P(x,y)} \tag{59}$$

is taken over all realisations of the tracer density field, and $P(x,y)$ denotes the bivariate p.d.f. of the tracer number density $x$ and the matter density $y$. The expression on the r.h.s. in the Eq. (58) is exact only for Gaussian statistics, which is assumed here as lowest-order approximation. For a differing statistics, such as a log-normal tracer density field (Coles & Jones 1991), we have to expect deviations from this expression. Evidently, the conditional average will vanish, if the correlation factor is $r^{(i)}(\ell) = 0$: the average tracer number density about a mass peak vanishes in this case.

According to this definition, the radial p.s.f. equals the average sight-line density profile (Eq. 77 of Simon et al. 2009):

$$\left[\bar{\boldsymbol{\delta}}_m(\Theta_s), \bar{\boldsymbol{n}}_g(\Theta_s)\right] = \int_0^\infty \frac{\mathrm{d}\ell\,\ell}{2\pi}\, \widetilde{F}(\ell\Theta_s)\, \widetilde{\mathsf{W}}_\ell \left[\tilde{\boldsymbol{\delta}}_m(\ell), \tilde{\boldsymbol{n}}_g(\ell)\right] \tag{60}$$

where the Wiener filter $\widetilde{\mathsf{W}}_\ell$ is given in Eq. (55), and the vectors $\tilde{\boldsymbol{\delta}}_m(\ell)$ and $\tilde{\boldsymbol{n}}_g(\ell)$ ($N_{lp}$ elements) vanish everywhere except in their $i$th element that equals 1 and $\bar{n}_g^{(i)} r^{(i)}(\ell) b^{(i)}(\ell)$, respectively. The elements of the vector $\bar{\boldsymbol{\delta}}_m(\Theta_s)$ encapsulate the radial p.s.f. of the matter map, and the radial p.s.f. of the tracer number density map in the case of $\bar{\boldsymbol{n}}_g(\Theta_s)$. The former is the focus in the following.

The resulting p.s.f. of the fiducial survey and a pixel size of $\Theta_s = 1$ arcmin is depicted in Fig. 2 for the cases $r(\ell) = 0, 0.8$. Owing to the Wiener smoothing, the mass peaks are generally radially smeared, and their amplitude is suppressed, in particular for very small and high redshifts. Compared to the lensing-only technique ($r(\ell) = 0$), however, adding tracers with $r \neq 0$ to the map making process, clearly improves the p.s.f.: the radial profiles are narrowed and more pronounced, the amplitudes are less suppressed. As the S/N in the map is improved as well, see left panel of Fig. 1, the redshift accuracy in the map also improves. The redshift accuracy is basically determined by how well the smoothed profiles of mass peaks at different redshifts can be distinguished considering the noise in the maps (see Sect. 2.6 in Simon et al. 2012). More importantly, the positions of smeared peaks now coincide with the redshifts of the peaks in the un-smoothed map. Therefore, a moderate mix of 3D lensing and galaxy clustering information potentially lifts the $z$-shift bias. This is explored in more detail by Fig. 3, where we find essentially no $z$-shift bias for $r(\ell) \ge 0.4$.

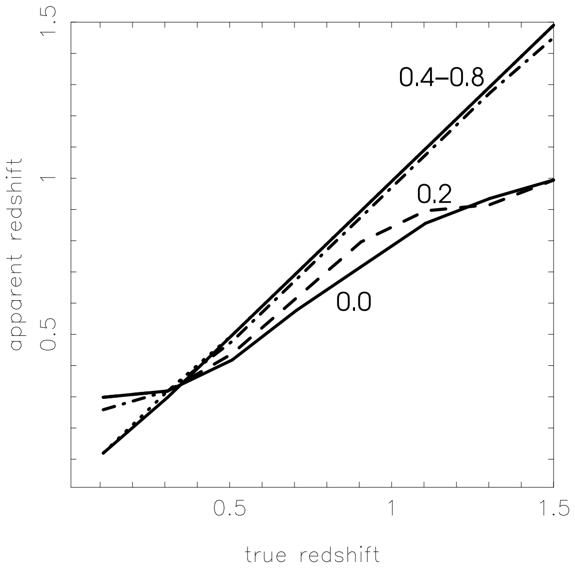

**Fig. 3.** Peak redshifts of the profiles of smeared mass peaks (ordinate) in comparison to the true peak redshifts (abscissa) for different correlation factors: $r(\ell) = 0$ (solid), $r(\ell) = 0.2$ (dashed), $r(\ell) = 0.4$ (dashed-dotted), $r(\ell) = 0.6, 0.8$ (indistinguishable diagonal lines).

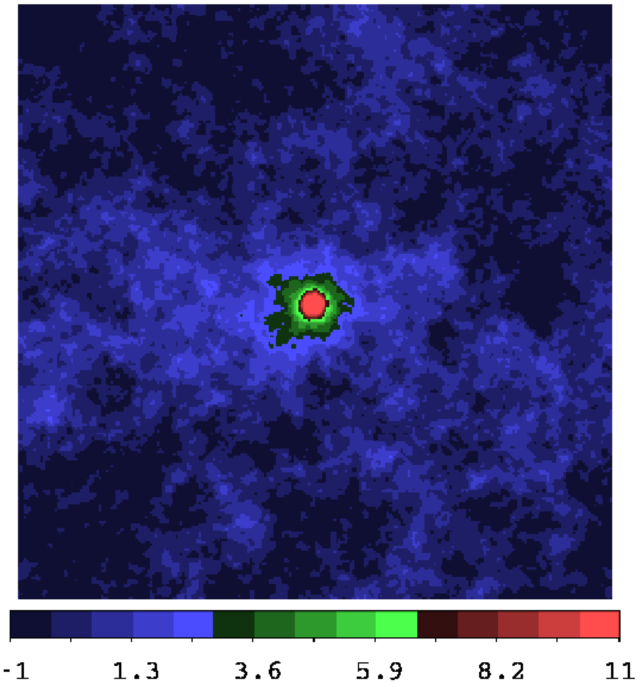

**Fig. 4.** Example of a constrained realisation of the tracer density contrast $\kappa_{\rm g}$ on a pixelised lens plane at redshift $z = 0.45$. The size of the figure is $1 \times 1\,{\rm deg}^2$ with $256 \times 256$ pixels. At the centre is a simulated mass peak with SIS density profile and $M_{200} = 6.6 \times 10^{14}\,M_\odot h^{-1}$. The adopted correlation between tracer number density and matter density is $r(\ell) = 0.8$. The bias factor is $b(\ell) = 1$.

### *4.4. Mock data 3D reconstruction*

As a demonstration of the mapping algorithm for a concrete 3D matter and galaxy number density field, we apply the new methodology to simple mock data with survey and binning parameters as described in Sect. 4.1. For the mocks, we place nine galaxy cluster scale mass peaks with a singular isothermal sphere (SIS) density profile and mass $M_{200} = 6.6 \times 10^{14}\,h^{-1} M_\odot$ (SIS velocity $\sigma_{\rm v} = 10^3\,{\rm kms}^{-1}$ at $z = 0$) on a regular angular grid that covers $A_{\rm fov} = 1 \times 1\,{\rm deg}^2$ with $256 \times 256$ pixels. The peaks are situated at the lens plane redshifts $z = 0.15, 0.25,$ etc.. For more details, we refer the reader to Simon et al. (2009) where similar mock data was produced.

We convert the model SIS mass density contrast on the lens planes, $\boldsymbol{\delta}_{\rm m}$, into pixelised shear fields $\boldsymbol{\gamma} = \mathsf{P}_{\gamma\kappa}\mathsf{Q}\boldsymbol{\delta}_{\rm m}$ according to Sect. 2.1. Then, we randomly draw source galaxy positions $\boldsymbol{\theta}_j$ and for each source random intrinsic ellipticities $\epsilon^{\rm i}$ to obtain the final mock catalogue source ellipticity $\gamma^{(i)}(\boldsymbol{\theta}_j) + \epsilon^{\rm i}$. The number of sources of each source redshift bin is determined by the total source number, $\overline{n}A_{\rm fov} \sim 10^5$, and the redshift distribution $p_z(z)$.

Every lens plane grid $\boldsymbol{\delta}^{(i)}_{\rm m}$ serves as input for a constrained realisation of the tracer number density $\boldsymbol{n}^{(i)}_{\rm g}$. As the correlation between matter and galaxy number density is not supposed to be perfect, here $r^{(i)}(\ell) = 0.8$, we have to simulate some additional, statistically independent scatter of the tracer density about the matter density. For the scope of this demonstration, we assume Gaussian statistics for the tracer density contrast

$$\kappa^{(i)}_{\rm g}(\boldsymbol{\theta}) = \frac{n^{(i)}_{\rm g}(\boldsymbol{\theta})}{\overline{n}^{(i)}_{\rm g}} - 1\;. \tag{61}$$

In this simplified case, a constrained realisation of $\boldsymbol{\kappa}^{(i)}_{\rm g}$ is easily done in Fourier space for every Fourier coefficient $\tilde{\kappa}^{(i)}_{\rm g}(\boldsymbol{\ell})$ independently. The Fourier coefficients $\tilde{f}(\boldsymbol{\ell})$ of a Gaussian random field are independent from each other. The bivariate p.d.f. of the Fourier coefficients of the tracer and matter field is

$$P\left(\tilde{\kappa}_{\rm g}, \tilde{\delta}_{\rm m}\right) = \frac{1}{2\pi\sigma^2 b\sqrt{1-r^2}}\exp\left(-\frac{\tilde{\kappa}^2_{\rm g}/b^2 + \tilde{\delta}^2_{\rm m} - 2r\tilde{\kappa}_{\rm g}\tilde{\delta}_{\rm m}/b}{2\sigma^2(1-r^2)}\right), \tag{62}$$

where $\sigma^2 = \langle\tilde{\delta}^2_{\rm m}\rangle$ is the variance of the matter density field, $[b, r]$ are the bias parameters, and all means $\langle\tilde{\kappa}_{\rm g}\rangle = \langle\tilde{\delta}_{\rm m}\rangle = 0$ vanish. In this context, by $\{\tilde{\delta}_{\rm m}, \tilde{\kappa}_{\rm g}\}$ we mean either the real or imaginary part of the Fourier coefficients. The imaginary and real parts are realised independently of each other. The conditional p.d.f. of $\tilde{\kappa}_{\rm g}$ for a given $\tilde{\delta}_{\rm m}$,

$$P\left(\tilde{\kappa}_{\rm g}|\tilde{\delta}_{\rm m}\right) = \frac{P\left(\tilde{\kappa}_{\rm g}, \tilde{\delta}_{\rm m}\right)}{P\left(\tilde{\delta}_{\rm m}\right)}\;, \tag{63}$$

is therefore also a Gaussian, namely with mean

$$\left\langle\tilde{\kappa}_{\rm g}\middle|\tilde{\delta}_{\rm m}\right\rangle = \int {\rm d}\tilde{\kappa}_{\rm g}\,P\left(\tilde{\kappa}_{\rm g}|\tilde{\delta}_{\rm m}\right)\tilde{\kappa}_{\rm g} = br\,\tilde{\delta}_{\rm m} \tag{64}$$

and variance

$$\sigma\left(\tilde{\kappa}_{\rm g}|\tilde{\delta}_{\rm m}\right) = \int {\rm d}\tilde{\kappa}_{\rm g}\,P\left(\tilde{\kappa}_{\rm g}|\tilde{\delta}_{\rm m}\right)\tilde{\kappa}^2_{\rm g} = b\sqrt{1-r^2}\,\sigma\;. \tag{65}$$

The variance in $\tilde{\delta}_{\rm m}$ is

$$\sigma^2 = \frac{P_\delta(\ell)}{2A_{\rm fov}}\;, \tag{66}$$

where $P_\delta(\ell)$ is the power spectrum of the matter density contrast on the lens plane, here determined by the matter distribution of

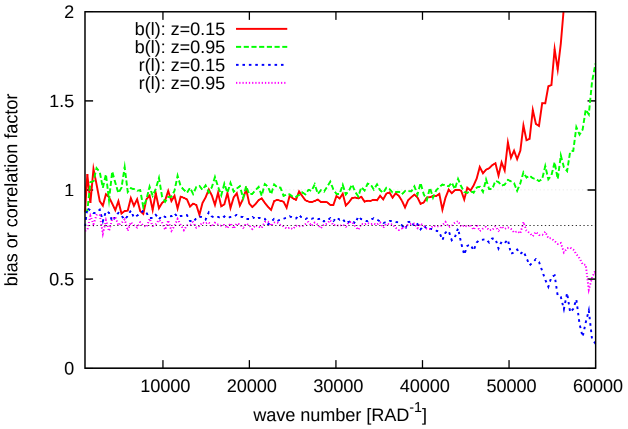

**Fig. 5.** Impact of clipping values in the realisations of tracer number density fields, as demonstrated by a particular realisation of the lens planes redshifts $z = 0.15, 0.95$. The bias and correlation factors become scale-dependent, most notably at low redshift, as opposed to the desired constant fiducial values of $b(\ell) = 1$ and $r(\ell) = 0.8$ (black horizontal lines). The relative error is below $\sim 10\%$ for $\ell \lesssim 5 \times 10^4 \cong 0.4$ arcmin.

the SIS. A realisation of $\tilde{\kappa}_{\rm g}(\boldsymbol{\ell})$ from a given $\tilde{\delta}_{\rm m}(\boldsymbol{\ell})$ is hence obtained by

1. multiplying $\tilde{\delta}_{\rm m}(\boldsymbol{\ell})$ by $b(\ell)\sqrt{1 - r(\ell)^2}$, which gives $\tilde{f}(\boldsymbol{\ell})$;
2. randomising the phases of the former product $\tilde{f}(\boldsymbol{\ell})$;
3. and adding $b(\ell)r(\ell)\tilde{\delta}_{\rm m}(\boldsymbol{\ell})$ to $\tilde{f}(\boldsymbol{\ell})$ to yield $\tilde{\kappa}_{\rm g}(\boldsymbol{\ell})$.

The entire grid of $\tilde{\kappa}_{\rm g}(\boldsymbol{\ell})$ obtained this way is then Fourier transformed into $\kappa_{\rm g}(\boldsymbol{\theta})$, taking into account the constraint $\tilde{\kappa}_{\rm g}(\boldsymbol{\ell}) = \tilde{\kappa}^*_{\rm g}(-\boldsymbol{\ell})$ for a real-valued tracer number density contrast.

In the final step, we convert every realisation of $\kappa_{\rm g}(\boldsymbol{\theta})$, such as the one in Fig. 4, into galaxy catalogues by drawing $N = \overline{n}_{\rm g}A_{\rm fov}$ random galaxy positions. For thus purpose, a uniformly drawn position $\boldsymbol{\theta}_j$ is accepted, if $1 + \kappa_{\rm g}(\boldsymbol{\theta}_j) \geq (1 + \kappa_{\rm g,max})x_{\rm rnd}$, where $\kappa_{\rm g,max}$ is the maximum of $\kappa_{\rm g}(\boldsymbol{\theta})$ and $x_{\rm rnd} \in [0, 1]$ is an additional random number from a uniform p.d.f. As redshift of a galaxy, we choose the lens plane redshift $z_i$ and add a random Gaussian redshift error with r.m.s. variance $\sigma_z(z_i) = 0.04(1 + z_i)$.

Owing to the Gaussianity of $\kappa_{\rm g}$ in this algorithm, we also find pixels with $1 + \kappa_{\rm g}(\boldsymbol{\theta}) < 0$, which formally corresponds to negative galaxy number densities. Since the algorithm treats such pixels equally as pixels with $\kappa_{\rm g} + 1 = 0$, we thereby clip all values smaller than $\kappa_{\rm g} < -1$. This introduces a small bias, such that the tracer power spectrum, $b^2(\ell)P_\delta(\ell)$, has not exactly the desired $b(\ell) = 1$ on small angular scales, especially at low redshifts where the density fluctuations are large (Fig. 5). Furthermore, there is a decorrelation, $r(\ell) < 0.8$, for large $\ell$. However, the relative error in the bias parameters is less than $\sim 10\%$ for scales larger than 1 arcmin, which is the angular smoothing scale in the following 3D maps.

We apply the reconstruction algorithm to the mock data in two different ways:

1. In the first application, only the 3D lensing data is invoked for a 3D matter density map, which is equivalent to setting $r^{(i)}(\ell) = 0$ for all lens planes in the Wiener filter. As tuning parameter, we choose $\alpha = 0.05$, thus slightly more Wiener smoothing than in the foregoing discussion. This was necessary to attain also mass peak detections at $z \gtrsim 0.3$ in the mock data.
2. In the second run, we mix the lensing and the galaxy clustering data with known biasing parameters in order to obtain an updated matter density map, this time with $\alpha = 0.01$ and $\beta = 0.1$.

In both cases, the density fields on the lens planes are smoothed with a Gaussian kernel of $\Theta_{\rm s} = 1$ arcmin r.m.s. size. Furthermore, both maps are divided by the pixel r.m.s. noise variance, which we compute from $10^3$ noise realisations. We produce the noise maps by first randomising the source ellipticities and the positions of the tracer galaxies, then followed by rerunning the map making algorithm. The resulting S/N maps are shown in Fig. 6. We do not attempt to correct for the $z$-shift bias in either case.

With lensing only (top row), we are most sensitive to structure at low redshift, but quickly loose detection capability at larger radial distances, even with increased Wiener smoothing. This example highlights the general problems with the Wiener mapping, namely the radial elongation of mass peaks and the $z$-shift bias, both originating from the radial p.s.f.[4] In the combined reconstruction (bottom row), we now recover features both with overall higher significance and clearly reduced radial stretch, and also significant features at higher redshifts. As a matter of fact, the significance increases again at high redshifts, presumably thanks to the increasing tracer number density until $z \sim 0.9$. Moreover, the mass peaks are very close to their true redshift, which indicates both a reduced $z$-shift bias and an increase in the map redshift accuracy.

### 4.5. Galaxy clustering noise

The noise realisations of the data in the foregoing section are incomplete, as they only account for the source shape noise and the tracer shot-noise. In the presence of stochasticity between matter and tracer density, $r(\ell) \neq 1$, there is a random scatter in the tracer density for a given matter density field, which enters the reconstructed matter map as additional noise component. Contrary to Poisson shot-noise, this noise component ("galaxy clustering noise" or GCN hereafter) is also present, if the number of tracer galaxies were infinite, and it has, in general, not a white-noise power spectrum.

As can be seen in Sect. 4.4 on the generation of mock data, for a given matter density $\tilde{\delta}_{\rm m}(\boldsymbol{\ell})$ a random component with power spectrum $b^2(\ell)[1 - r^2(\ell)]P_\delta(\ell)$ is added to produce a realisation of the tracer number density $\tilde{n}_{\rm g}(\boldsymbol{\ell})$, which is the GCN in the *Gaussian* case. The essential parameter for this random scatter is $r(\ell)$, which for $|r(\ell)| = 1$ vanishes, but reaches a maximum in amplitude for $r(\ell) = 0$. On the other hand, a smaller $r(\ell)$ also results in a reduction of the mixing of matter and tracer density modes by the minimum-variance filter. On the extreme end for $r(\ell) = 0$, the filter will not make use of any tracer information at all for the matter density map.

For an assessment of the level of the GCN, we assume an idealised survey with Gaussian statistics and estimate the power of the noise that passes through the filter in comparison to the signal power in the mass map. The total noise power per angular mode in the mass map can then be approximated by

$$\mathsf{P}_{\rm n,all}(\ell) := \mathsf{P}_{\rm n}(\ell) + \mathsf{P}_{\rm gcn}(\ell)\,, \tag{67}$$

---

[4] The $z$-shift bias in a S/N map generally differs from the $z$-shift bias in the matter density map (Simon et al. 2012).

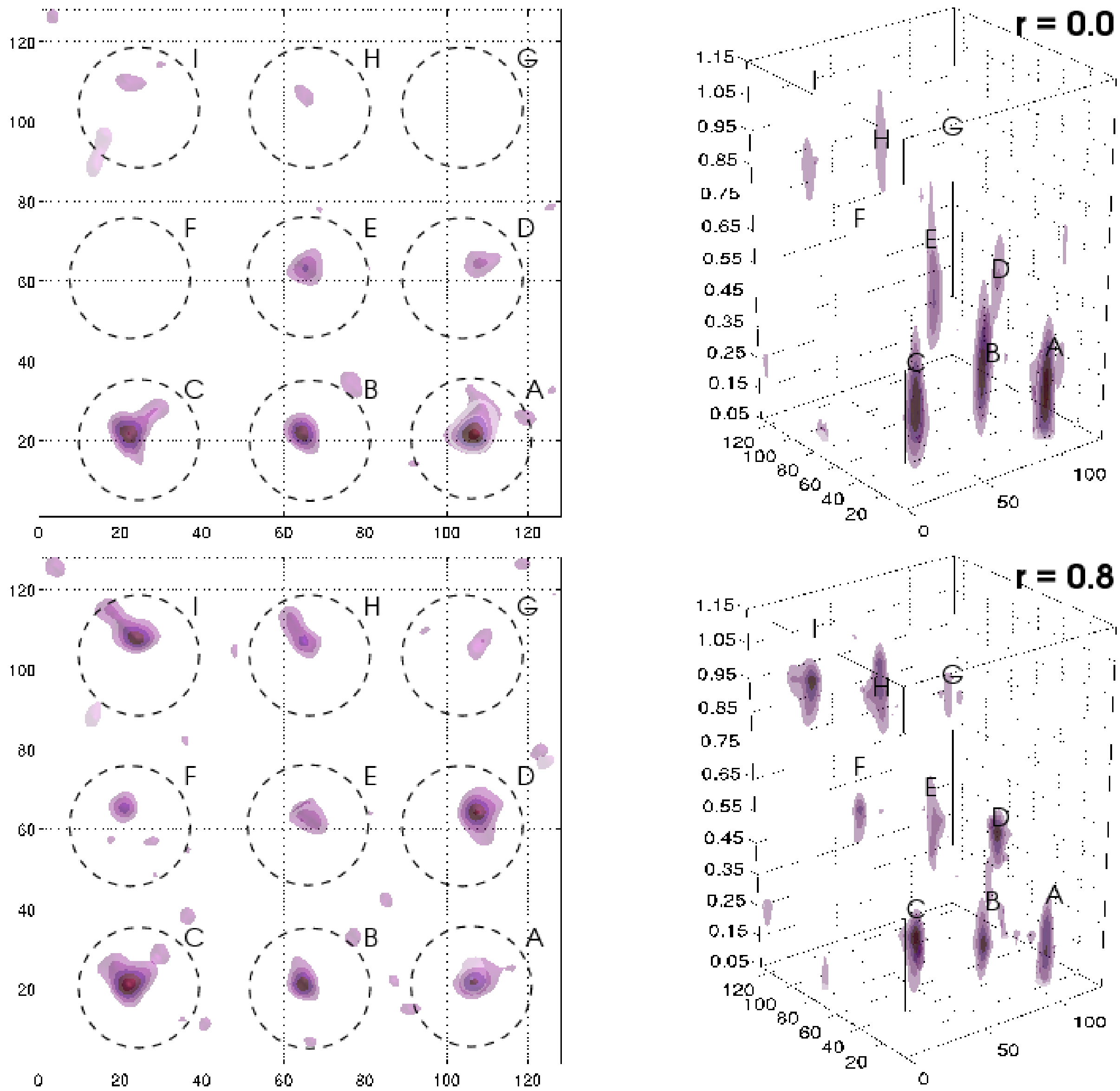

**Fig. 6.** S/N map of the matter density field by either utilising the lensing catalogue only (top row; $\alpha = 0.05$), or by mixing lensing and galaxy clustering data with $r(\ell) = 0.8$ and $b(\ell) = 1$ (bottom row; $\alpha = 0.01, \beta = 0.1$). The right column shows a radial projection, values varying between 0.05 and 1.15 are the lens plane redshifts. The left column panels are the corresponding projection on the sky ($1 \times 1\,\mathrm{deg}^2$). The circles circumscribe the positions of nine SIS mass peaks with $M_{200} = 6.6 \times 10^{14} M_\odot h^{-1}$ and at increasing redshift $z = 0.15, 0.25$, etc.. The shadowed areas are projected iso-surfaces of S/N = 3, 4, . . ..

where $\mathsf{P}_{\rm n}(\ell)$ quantifies the tracer shot-noise and source shape-noise inside the map, see Eq. (54), and the GCN after the application of the Wiener filter $\widetilde{\mathsf{W}}_\ell$ is

$$\mathsf{P}_{\rm gcn}(\ell) := \widetilde{\mathsf{W}}_\ell \widetilde{\mathsf{S}}^{\rm gcn}_\ell \widetilde{\mathsf{W}}^\dagger_\ell\,, \tag{68}$$

where

$$\widetilde{\mathsf{S}}^{\rm gcn}_\ell := \tag{69}$$

$$\mathrm{diag}\left\{\underbrace{0,\dots,0,}_{\mathrm{N_{lp}\ elements}}[\overline{n}^{(1)}_{\rm g}]^2 P^{(1)}_{\rm gcn}(\ell),\dots,[\overline{n}^{(N_{\rm lp})}_{\rm g}]^2 P^{(N_{\rm lp})}_{\rm gcn}(\ell)\right\}\,,$$

and the Gaussian GCN in the un-smoothed map is

$$P^{(i)}_{\rm gcn}(\ell) = \left[b^{(i)}(\ell)\right]^2 \left(1 - [r^{(i)}(\ell)]^2\right) P^{(i)}_\delta(\ell)\,. \tag{70}$$

For the previous fiducial survey and for $r(\ell) \in [0, 1.0]$ and $b(\ell) \in [0, 3.0]$, we find that the GCN is smaller than $\sim 30\%$ of the actual signal $\mathsf{P}_{\rm s}$ in the map (Fig. 7) for angular modes larger than $\sim 1$ arcmin. For this estimate, we take the cosmic average $P^{(i)}_\delta(\ell)$ as the signal power in the un-smoothed matter density field. This certainly underestimates the fluctuations in the relevant galaxy cluster regions. On the other hand, the GCN scales, at least for Gaussian random fields, linearly with the amplitude of the actual matter density fluctuations, Eq. (70), such that the GCN-to-signal ratio in Fig. 7 should still be a robust approximation for Gaussian fields with more matter clustering. We find the GCN in the smoothed maps to be most prominent for $r(\ell) \sim 0.6$, declining for correlations greater or weaker than that. The GCN increases with the clustering $b(\ell)$ of the tracers and declines for angular modes with wave-numbers greater than $\ell \sim 3 \times 10^3$ ($\sim 7$ arcmin).

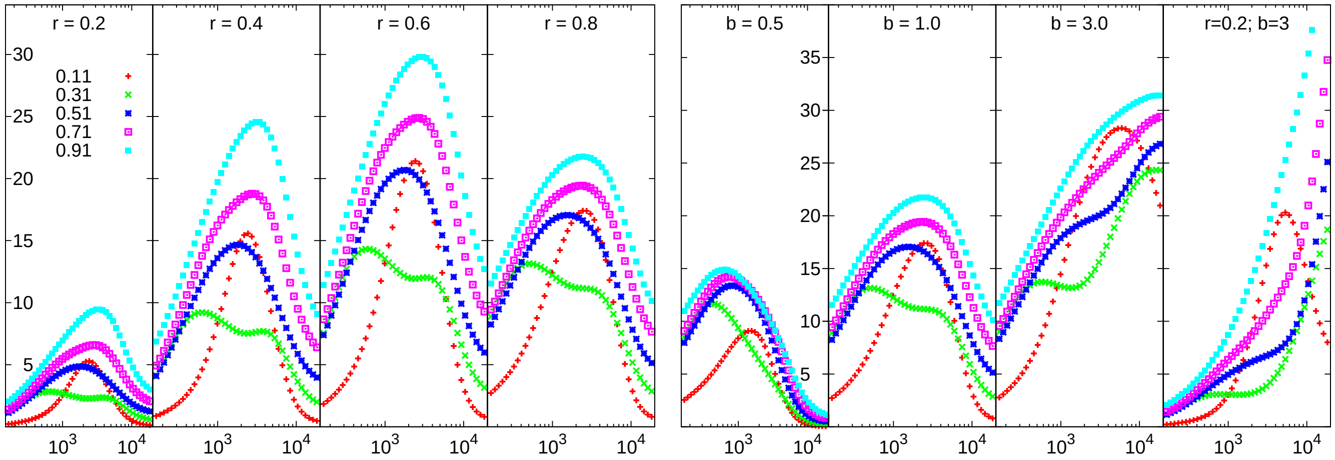

**Fig. 7.** Estimated percentage GCN-to-signal ratio $\mathsf{P}_{\rm gcn}(\ell)/\mathsf{P}_{\rm s}(\ell)$ ($y$-axis) as function of lens plane redshift (different data points) and angular wave-number ($x$-axis). The tuning parameters are $\alpha = 0.01$ and $\beta = 0.1$. *Left:* The bias factor is set to $b(\ell) = 1$, different panels correspond to different correlation factors $r(\ell)$. *Right:* Varying bias factors (panels), while keeping the correlation factor at $r(\ell) = 0.8$. There is one exception in the very right panel that depicts a strong GCN level for $r(\ell) = 0.2$ and $b(\ell) = 3.0$.

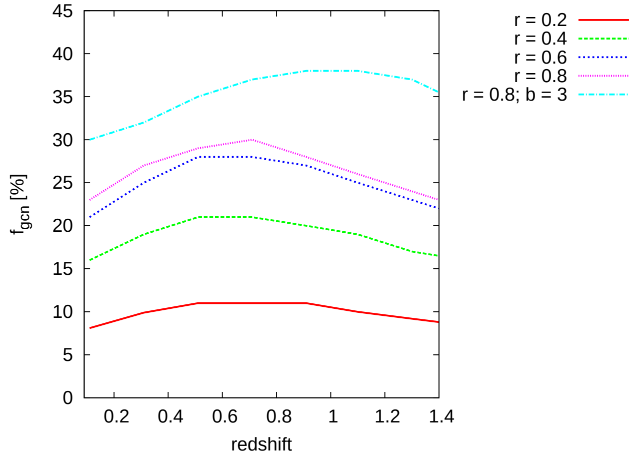

**Fig. 8.** GCN variance $f_{\rm gcn}$ on a pixel scale of $\Theta_{\rm s} = 1$ arcmin radius relative to the signal variance in the fiducial survey as function of lens plane redshift. The lines differ in their assumed $r(\ell)$. Except for one line (indicated), the bias factor of the tracers is $b(\ell) = 1$.

For each lens plane, we translate these $\ell$-dependent GCN levels to the noise variance on the map pixel scale by virtue of the integral (Simon et al. 2009)

$$\left\langle[\delta^{(i)}_{\rm gcn}(\Theta_{\rm s})]^2\right\rangle = \int_0^\infty \frac{{\rm d}\ell\,\ell}{2\pi}|\widetilde{F}(\ell\Theta_{\rm s})|^2[\mathsf{P}_{\rm gcn}(\ell)]_{ii}\,, \tag{71}$$

and likewise for the signal power $[\mathsf{P}_{\rm s}(\ell)]_{ii}$ in Eq. (53) to compute $\langle[\delta^{(i)}_{\rm s}(\Theta_{\rm s})]^2\rangle$. Fig. 8 shows the resulting GCN-to-signal ratios

$$f^{(i)}_{\rm gcn} = \sqrt{\frac{\langle[\delta^{(i)}_{\rm gcn}(\Theta_{\rm s})]^2\rangle}{\langle[\delta^{(i)}_{\rm s}(\Theta_{\rm s})]^2\rangle}} \tag{72}$$

for pixels in our fiducial mass map. Typical figures for $f^{(i)}_{\rm gcn}$ are below 30%, but can go above this level for strongly clustered tracers. The exact value of $f^{(i)}_{\rm gcn}$ depends on the survey and Wiener filter parameters, which can be determined by the above formalism. Once $f^{(i)}_{\rm gcn}$ has been determined, the S/N levels in every lens plane of a map, such as Fig. 6, can in principle be rescaled by the following recipe to incorporate the GCN.

The pixel-to-pixel variance $\sigma^2_{\rm all}$ in a mass map has three independent components,

$$\sigma^2_{\rm all} = \sigma^2_{\rm s} + \sigma^2_{\rm gcn} + \sigma^2_{\rm shot} = \left(1 + f^2_{\rm gcn}\right)\sigma^2_{\rm s} + \sigma^2_{\rm shot}\,, \tag{73}$$

where $\sigma_{\rm s}$ is the variance in the matter density signal, $\sigma_{\rm gcn}$ is the GCN variance, and $\sigma_{\rm shot}$ is the source shape- and tracer shot-noise variance. In the former equation, we have substituted the GCN variance by the signal variance and the GCN-to-signal ratio $f_{\rm gcn}$. A S/N map that accounts for both $\sigma_{\rm shot}$ and $\sigma_{\rm gcn}$ is

$$\frac{\delta_{\rm m,est}(\boldsymbol{\theta})}{\sqrt{\sigma^2_{\rm shot} + \sigma^2_{\rm gcn}}} = \tag{74}$$

$$\frac{\delta_{\rm m,est}(\boldsymbol{\theta})}{\sigma_{\rm shot}}\left(1 + \frac{\sigma^2_{\rm gcn}}{\sigma^2_{\rm shot}}\right)^{-1/2} = \frac{\delta_{\rm m,est}(\boldsymbol{\theta})}{\sigma_{\rm shot}} \times \left(1 + f^2_{\rm gcn}\frac{\sigma^2_{\rm s}}{\sigma^2_{\rm shot}}\right)^{-1/2}\,,$$

where $\delta_{\rm m,est}(\boldsymbol{\theta})/\sigma_{\rm shot}$ on the right-hand side (r.h.s.) is the S/N invoking shot-noise only, such as the bottom panel of Fig. 6. For the correction factor inside the brackets, the signal variance $\sigma_{\rm shot}$ can be estimated by employing Eq. (71) with an appropriate Wiener-filtered signal power spectrum. In addition, the shot-noise variance, $\sigma_{\rm s}$, is determined by the pixel variance in the noise realisations, or also by Eq. (71) with the Wiener filter noise power spectrum $\mathsf{P}_{\rm n}(\ell)$ inside the integral. For a signal variance $\sigma_{\rm s} \ll \sigma_{\rm shot}$, the correction factor is roughly unity, which is always the case for a cosmic average matter density power spectrum and our fiducial survey.

As we are mainly targeting galaxy cluster regions with lensing cartography, however, a fiducial value of $\sigma_{\rm s}$ of higher variance than in a cosmic average is likely. To obtain a more reasonable fiducial value, we construct for $\sigma_{\rm s}$ an alternative signal power spectrum, based on the assumption of (i) randomly scattered haloes with average number density $\overline{n}_{\rm sis}$ and (ii) haloes with a SIS matter density profile[5] (Simon et al. 2009)

$$\tilde{\delta}^{(i)}_{\rm sis}(\ell) = \frac{8\pi^2}{3\Omega_{\rm m}[1+z(\overline{\chi}_i)]}\left(\frac{\sigma_{\rm v}}{c}\right)^2 \frac{D_{\rm H}^2}{f_{\rm K}(\overline{\chi}_i)\Delta\chi_i}\frac{1}{\ell}\;. \tag{75}$$

in Fourier space and SIS velocity $\sigma_{\rm v}$. Therefore, the matter power spectrum for the $i$th lens plane is described by (Appendix A)

$$P^{(i)}_{\delta}(\ell) = |\tilde{\delta}^{(i)}_{\rm sis}(\ell)|^2\overline{n}_{\rm sis}\;, \tag{76}$$

which we insert into Eq. (53) and Eq. (71) to calculate $\sigma_{\rm s}$. In accordance with our mock data, we use $\overline{n}_{\rm sis} = 1\,{\rm deg}^{-2}$ and $\sigma_{\rm v} = 10^3\,{\rm km s}^{-1}$, which actually is a conservative upper limit since the SIS velocity of the mass peaks in the simulation decreases with redshift due to the fixed $M_{200}$ mass. We find that for $r(\ell) = 0.8$ and $b(\ell) = 1$ the S/N levels in Fig. 6 have to be reduced to $\sim 75\%, 90\%$ at $z = 0.15, 0.25$ and to values $\gtrsim 93\%$ otherwise. These figures are roughly lower limits for $r(\ell) \in [0,1]$ and $b(\ell) \in [0,3]$. This qualitatively matches our observation in the mock data that there are only extra features at low redshift in the combined reconstruction.

### *4.6. Mismatched biasing parameters*

In the foregoing discussion, we have always assumed that the Wiener filter devises a set of galaxy biasing parameters that exactly matches the biasing inside the data. More generally, however, we may also use biasing parameters for the Wiener smoothing (Step-2 in Eq. 41),

$$\mathsf{B} := \left(1+\mathsf{SN}^{-1}_{\delta n_{\rm g}}\right)^{-1}\mathsf{SN}_{\delta n_{\rm g}}\;, \tag{77}$$

that are different from the biasing in the data (mismatched), as long as we devise for the forgoing analysis of the radial p.s.f. and the S/N map the correct parameter set for the actual galaxy biasing in the data; we would thus have different values for $[b(\ell), r(\ell)]$ in $\widetilde{\mathsf{W}}_\ell$ and $\widetilde{\mathsf{S}}_\ell$ in Eq. (53).

In a practical application, we may deliberately decide in favour of mismatched values of $r(\ell)$ by choosing a value in the filter $\mathsf{B}$ just high enough to apply sufficient mixing of matter and tracer density modes to lift the $z$-shift bias.

As extreme example for the impact of wrong bias parameters, consider the case that we adopt $r(\ell) = 0.8$ for the Wiener filter and assume the same value for the data, although we have no correlation between the matter and galaxy distribution in the data to which the Wiener filter applies, i.e., $\langle\tilde{\kappa}_{\rm g}|\tilde{\delta}_{\rm m}\rangle = 0$ instead of $\langle\tilde{\kappa}_{\rm g}|\tilde{\delta}_{\rm m}\rangle = br\tilde{\delta}_{\rm m}$ (Sect. 4.4). If this is ignored, we will arrive with Eq. (60) at the conclusion that the right panel of Fig. 2 is the p.s.f. inside the matter map instead of a p.s.f. very similar to the left panel (not shown), which exhibits a clear $z$-shift bias. Moreover, we will underestimate the level of GCN and hence overestimate the S/N levels in the map, which will lead to an increase of false positive detections in the map.

### *4.7. Non-Gaussianities*

For the GCN, a great uncertainty is the true nature of the galaxy biasing, which up to here has been treated as Gaussian, such that a linear stochastic biasing model is a complete description of galaxy biasing. Although this is probably a fair description for large smoothing scales beyond $\sim 8\,h^{-1}$Mpc, it is increasingly inaccurate at smaller scales where the biasing is expected to become non-linear (e.g., Yoshikawa et al. 2001). As immediate consequence, the Gaussian GCN analysis above probably underestimates the clustering noise on small angular scales. The detection rate of false positives in the mass map would rise as a consequence.

Moreover, non-linearities in the biasing may have unwanted side-effects, such as a mass map being strongly skewed towards the galaxy distribution. This may be illustrated by the high-peak bias model (Kaiser 1984; Bardeen et al. 1986), which is non-linear and deterministic. In this model, galaxies are found inside peaks of the matter density field that exceed a certain density threshold (“high-peaks”); outside those peaks, the galaxy number density is exactly zero. This model is deterministic, as it assumes the same $\boldsymbol{n}_{\rm g}$ for a given $\boldsymbol{\delta}_{\rm m}$. Nevertheless, the correlation factor is not exactly $r(\ell) = 1$, since the galaxy number density always vanishes outside the high-peaks, even though the matter density may be varying. Due to $r(\ell) \neq 0$, there is a linear mixing of tracer and matter density modes in the Wiener filter which, however, suppresses the matter density outside the high-peaks, since there we have $\kappa_{\rm g} = -1$. The mass map outside the high-peaks is probably underrepresented as a result. We have shown that the Wiener filter is biased by construction, as it is applying smoothing to the maps. But this example shows that the exact appearance of the bias also depends on the details of the galaxy biasing mechanism. It is likely that for a more accurate mapping algorithm on non-linear scales, a more elaborate modelling of the statistics and the detailed galaxy biasing is required, perhaps in the vein of Jasche et al. (2010) but also incorporating lensing.

## 5. Summary and conclusions

In this study, we introduce and discuss a new technique for the synergy of lensing and galaxy clustering information in order to map the 3D matter density. This technique devises a minimum-variance filter based upon both the 3D shear information from radially binned sources and the angular distribution of a coarsely binned galaxy tracer population with possibly inaccurate redshifts. The filter essentially proceeds in two steps: Step-1 produces an unbiased estimate of the matter and tracer number density, while Step-2 linearly combines both to produce smoothed density fields with an enhanced S/N. The estimator becomes biased through Step-2, but it is consistent as it becomes asymptotically unbiased when the S/N in the data approaches infinity. The smoothing of the maps is uniquely defined in Eq. (77), which and can be applied to theoretical maps of the matter and galaxy number density for a quantitative comparison to the data.

As novelty, the filter linearly mixes the matter and galaxy (tracer) number density with a weighting that depends on the galaxy bias of the tracer population. In principle, the biasing parameters can be constrained from the data itself by using lensing techniques (cf., Hoekstra et al. 2002; Simon 2012). In a situation, where the tracers have no statistical correlation to the matter density field, there is no mixing and hence no gain from a synergy. The level of smoothing and mixing is regulated by two independent tuning parameters that rescale the noise covariance inside the filter.

For the discussion of the filter, we assume a fiducial survey with mean redshift $\overline{z} = 0.84$, a source number density of $\overline{n} = 30$ galaxies per arcmin$^2$, in accordance with Simon et al. (2009), and a tracer number density of $\overline{n}_{\rm g} = 3$ galaxies per arcmin$^2$ that is almost unbiased but has some stochasticity (Sect. 4.4). Most of the information on the matter density originates from the clustering of the tracer population, at least when the biasing is exactly known. We have chosen to keep the influence of the tracer density maps on the mass map at a low level by artificially reducing the S/N level of the tracers in the Wiener filter, which is done by appropriately choosing the tuning parameters ($\alpha = 0.01$, $\beta = 0.1$). Moreover, in future applications, the mixing could additionally be reduced by adopting a correlation factor inside the Wiener filter that is smaller than the actual correlation in the data.

---

[5] The formalism in Sect. 2.1 is built around the mean density contrast $\delta^{(i)}_{\rm m}(\boldsymbol{\theta})$ within a volume slice of width $\Delta\chi$, whereas the SIS density contrast is commonly written as integrated contrast along a l.o.s.; the difference between both definitions is the factor $\Delta\chi$.

The S/N in the matter density map is improved by the synergy, especially at higher redshifts. However, at our adopted level of mixing, significant detections are basically still restricted to peaks of a galaxy cluster mass scale. By quantifying the average radial smoothing kernel or p.s.f. in the map, we have shown that the most useful improvement of a synergy is a removal of the $z$-shift bias, which is known from lensing-only methodologies based on linear filters. Even for relatively moderate levels of correlation between the matter and tracer density, $r \gtrsim 0.4$, the $z$-shift bias is removed from the mass map. Likewise, the peaks in the mass map are also less radially smeared out owing to the narrower radial p.s.f., in particular for high correlation factors. An increase of the S/N and less smearing at the same time also results in a higher redshift accuracy of the mass peaks.

The synergy introduces a new kind of noise into the mass maps (galaxy clustering noise; GCN) that stems from a random scatter of the galaxy number density about a fixed matter density field (stochastic biasing). We derive estimates for the GCN in the Gaussian regime and show that it can relatively easy accounted for through rescaling the S/N maps that are obtained by randomising the source shapes and the galaxy tracer positions. For the fiducial survey discussed in the paper, this correction mainly affects the lens planes with $z \lesssim 0.3$.

The GCN discussion, however, assumes Gaussian statistics which only applies on large smoothing scales greater than $\sim 8\,h^{-1}$Mpc. On smaller scales, the statistics is likely to be more complex, possibly resulting in spurious false detections in the mass map whenever a Gaussian GCN model is used. Moreover, we argue that the detailed bias of the filter depends on the details of the galaxy biasing mechanism in the non-linear regime. More elaborate models or computer simulations are needed to investigate this effect.

## Acknowledgements

Patrick Simon acknowledges support by the European DUEL Research-Training Network (MRTN-CT-2006-036133) and the Deutsche Forschungsgemeinschaft in the framework of the Collaborative Research Center TR33 ‘The Dark Universe’

## References

Abdelsalam, H. M., Saha, P., & Williams, L. L. R. 1998, AJ, 116, 1541
Bacon, D. J. & Taylor, A. N. 2003, MNRAS, 344, 1307
Bardeen, J. M., Bond, J. R., Kaiser, N., & Szalay, A. S. 1986, ApJ, 304, 15
Bartelmann, M., Narayan, R., Seitz, S., & Schneider, P. 1996, ApJ, 464, L115
Bartelmann, M. & Schneider, P. 2001, Physics Reports, 340, 291
Bonnet, H., Mellier, Y., & Fort, B. 1994, ApJ, 427, L83
Bradač, M., Clowe, D., & Gonzalez, e. 2006, ApJ, 652, 937
Bradač, M., Schrabback, T., & Erben, e. 2008, ApJ, 681, 187
Bridle, S. L., Hobson, M. P., Lasenby, A. N., & Saunders, R. 1998, MNRAS, 299, 895
Broadhurst, T. J., Taylor, A. N., & Peacock, J. A. 1995, ApJ, 438, 49
Clowe, D., Bradač, M., & Gonzalez, A. H. e. 2006, ApJ, 648, L109
Clowe, D., Luppino, G. A., & Kaiser, e. 1998, ApJ, 497, L61
Clowe, D., Luppino, G. A., & Kaiser, e. 2000, ApJ, 539, 540
Coles, P. & Jones, B. 1991, MNRAS, 248, 1
Dahle, H., Pedersen, K., & Lilje, e. 2003, ApJ, 591, 662
Deb, S., Goldberg, D. M., Heymans, C., & Morandi, A. 2010, ApJ, 721, 124
Deriaz, E., Starck, J.-L., & Pires, S. 2012, `arXiv:1201.5214`
Dietrich, J. P., Schneider, P., & Clowe, D. e. 2005, A&A, 440, 453
Dodelson, S. 2003, Modern cosmology, ed. Dodelson, S.
Fan, Z. 2003, ApJ, 594, 33
Fischer, P. 1999, AJ, 117, 2024
Fischer, P. & Tyson, J. A. 1997, AJ, 114, 14
Gavazzi, R., Adami, C., & Durret, e. 2009, A&A, 498, L33
Guzik, J. & Seljak, U. 2001, MNRAS, 321, 439
Guzzo, L., Pierleoni, M., & Meneux, B. e. 2008, Nature, 451, 541
Heymans, C., Gray, M. E., Peng, C. Y., & et al. 2008, MNRAS, 385, 1431
Hirata, C. M. & Seljak, U. 2004, Phys. Rev. D, 70, 063526
Hoekstra, H., van Waerbeke, L., & Gladders, M. D. e. 2002, ApJ, 577, 604
Holhjem, K., Schirmer, M., & Dahle, H. 2009, A&A, 504, 1
Hu, W. 2002, Phys. Rev. D, 66, 083515
Hu, W. & Keeton, C. R. 2002, Phys. Rev. D, 66, 063506
Israel, H., Erben, T., Reiprich, T. H., et al. 2010, A&A, 520, A58
Jasche, J., Kitaura, F. S., Li, C., & Enßlin, T. A. 2010, MNRAS, 409, 355
Jee, M. J., Ford, H. C., & Illingworth, e. 2007, ApJ, 661, 728
Jee, M. J., White, R. L., & Benítez, N. e. 2005, ApJ, 618, 46
Jullo, E., Rhodes, J., Kiessling, A., et al. 2012, `arXiv:1202.6491`
Kaiser, N. 1984, ApJ, 284, L9
Kaiser, N. 1992, ApJ, 388, 272
Kaiser, N. 1995, ApJ, 439, L1
Kaiser, N. & Squires, G. 1993, ApJ, 404, 441
King, L. J., Clowe, D. I., & Lidman, e. 2002, A&A, 385, L5
Leonard, A., Dupé, F.-X., & Starck, J.-L. 2012, A&A, 539, A85
Lombardi, M., Rosati, P., & Nonino, e. 2000, A&A, 363, 401
Markevitch, M., Gonzalez, A. H., & Clowe, e. 2004, ApJ, 606, 819
Marshall, P. 2006, MNRAS, 372, 1289
Marshall, P. J., Hobson, M. P., Gull, S. F., & Bridle, S. L. 2002, MNRAS, 335, 1037
Martínez, V. J. & Saar, E. 2002, Statistics of the Galaxy Distribution, ed. Martínez, V. J. & Saar, E. (Chapman and Hall/CRC)
Massey, R., Rhodes, J., Ellis, R., & et al. 2007, Nat, 445, 286
Miyazaki, S., Hamana, T., & Shimasaku, e. 2002, ApJ, 580, L97
Okabe, N., Takada, M., Umetsu, K., Futamase, T., & Smith, G. P. 2010, PASJ, 62, 811
Pen, U.-L. 1998, ApJ, 504, 601
Pen, U.-L. 2004, MNRAS, 350, 1445
Pen, U.-L., Lu, T., van Waerbeke, L., & Mellier, Y. 2003, MNRAS, 346, 994
Reyes, R., Mandelbaum, R., & Seljak, U. e. 2010, Nature, 464, 256
Saini, T. D. & Raychaudhury, S. 2001, ApJ, 560, L9
Schirmer, M., Hildebrandt, H., Kuijken, K., & Erben, T. 2011, A&A, 532, A57
Schneider, P. 1995, A&A, 302, 639
Schneider, P. 1996, MNRAS, 283, 837
Schneider, P. 1998, ApJ, 498, 43
Schneider, P. 2006a, in Saas-Fee Advanced Course 33: Gravitational Lensing: Strong, Weak and Micro, ed. G. Meylan, P. Jetzer, P. North, P. Schneider, C. S. Kochanek, & J. Wambsganss, 1–89
Schneider, P. 2006b, in Saas-Fee Advanced Course 33: Gravitational Lensing: Strong, Weak and Micro, ed. G. Meylan, P. Jetzer, P. North, P. Schneider, C. S. Kochanek, & J. Wambsganss, 269–451
Schneider, P. & Seitz, C. 1995, A&A, 294, 411
Schrabback, T., Hartlap, J., & Joachimi, B. 2010, A&A, 516, 63
Seitz, C. & Schneider, P. 1995, A&A, 297, 287
Seitz, C. & Schneider, P. 1997, A&A, 318, 687
Seitz, S. & Schneider, P. 1996, A&A, 305, 383
Seitz, S. & Schneider, P. 2001, A&A, 374, 740
Seitz, S., Schneider, P., & Bartelmann, M. 1998, A&A, 337, 325
Simon, P. 2012, `arXiv:1202.2046`
Simon, P., Hetterscheidt, M., Schirmer, M., et al. 2007, A&A, 461, 861
Simon, P., Heymans, C., & Schrabback, e. 2012, MNRAS, 419, 998
Simon, P., Taylor, A. N., & Hartlap, J. 2009, MNRAS, 399, 48
Smail, I., Ellis, R. S., & Fitchett, e. 1995, MNRAS, 273, 277
Smith, R. E., Peacock, J. A., Jenkins, A., & et al. 2003, MNRAS, 341, 1311
Squires, G. & Kaiser, N. 1996, ApJ, 473, 65
Squires, G., Kaiser, N., & Babul, A. e. 1996a, ApJ, 461, 572
Squires, G., Kaiser, N., & Fahlman, G. e. 1996b, ApJ, 469, 73
Starck, J.-L., Pires, S., & Réfrégier, A. 2006, A&A, 451, 1139
Taylor, A. N., Bacon, D. J., Gray, M. E., & et al. 2004, MNRAS, 353, 1176
Tegmark, M. & Peebles, P. J. E. 1998, ApJ, 500, 79
Tyson, J. A. & Fischer, P. 1995, ApJ, 446, L55
Tyson, J. A., Wenk, R. A., & Valdes, F. 1990, ApJ, 349, L1
Umetsu, K. & Futamase, T. 2000, ApJ, 539, L5
van Waerbeke, L. 1998, A&A, 334, 1

VanderPlas, J. T., Connolly, A. J., Jain, B., & Jarvis, M. 2011, ApJ, 727, 118
Weinberg, D. H., Davé, R., & Katz, N. e. 2004, ApJ, 601, 1
Yoshikawa, K., Taruya, A., & Jing, Y. P. e. 2001, ApJ, 558, 520
Zaroubi, S., Hoffman, Y., & Fisher, K. B. e. 1995, ApJ, 449, 446

## Appendix A: SIS power spectrum

A set of $N_\mathrm{h}$ haloes with positions $\boldsymbol{\theta}_j$ on the $i$th lens plane, and an average, axial-symmetric matter density contrast $\delta_\mathrm{sis}(|\boldsymbol{\theta}|)$ produces the combined density contrast

$$\delta^{(i)}_\mathrm{m}(\boldsymbol{\theta}) = \sum_{j=1}^{N_\mathrm{h}} \delta_\mathrm{sis}(|\boldsymbol{\theta}-\boldsymbol{\theta}_j|)\;;\;\tilde{\delta}^{(i)}_\mathrm{m}(\boldsymbol{\ell}) = \tilde{\delta}_\mathrm{sis}(\ell)\sum_{j=1}^{N_\mathrm{h}} \mathrm{e}^{+\mathrm{i}\boldsymbol{\ell}\boldsymbol{\theta}_j}\;, \tag{A.1}$$

where the second equation on the r.h.s. is the Fourier transform of $\delta^{(i)}_\mathrm{m}(\boldsymbol{\theta})$. Averaging the two-point correlator of the density in Fourier space over all halo positions, results in

$$\left\langle\tilde{\delta}^{(i)}_\mathrm{m}(\boldsymbol{\ell}_1)\tilde{\delta}^{(i)}_\mathrm{m}(\boldsymbol{\ell}_2)\right\rangle = \tag{A.2}$$

$$\tilde{\delta}_\mathrm{sis}(\ell_1)\tilde{\delta}_\mathrm{sis}(\ell_2)\left[\sum_{j=1}^{N_\mathrm{h}}\left\langle\mathrm{e}^{+\mathrm{i}(\boldsymbol{\ell}_1+\boldsymbol{\ell}_2)\boldsymbol{\theta}_j}\right\rangle + \sum_{j\neq k=1}^{N_\mathrm{h}}\left\langle\mathrm{e}^{+\mathrm{i}\boldsymbol{\ell}_1\boldsymbol{\theta}_j}\mathrm{e}^{+\mathrm{i}\boldsymbol{\ell}_2\boldsymbol{\theta}_k}\right\rangle\right]\;.$$

We ignore the clustering of the haloes over the field-of-view $A_\mathrm{fov}$, so that the two-halo term in the second sum vanishes, and

$$\begin{aligned}\left\langle\tilde{\delta}^{(i)}_\mathrm{m}(\boldsymbol{\ell}_1)\tilde{\delta}^{(i)}_\mathrm{m}(\boldsymbol{\ell}_2)\right\rangle &= \tilde{\delta}_\mathrm{sis}(\ell_1)\tilde{\delta}_\mathrm{sis}(\ell_2)\sum_{j=1}^{N_\mathrm{h}}\frac{(2\pi)^2}{A_\mathrm{fov}}\delta_\mathrm{D}(\boldsymbol{\ell}_1+\boldsymbol{\ell}_2) && \text{(A.3)}\\ &= (2\pi)^2\delta_\mathrm{D}(\boldsymbol{\ell}_1+\boldsymbol{\ell}_2)\,\tilde{\delta}_\mathrm{sis}(\ell_1)\tilde{\delta}_\mathrm{sis}(\ell_2)\overline{n}_\mathrm{sis} && \text{(A.4)}\\ &= (2\pi)^2\delta_\mathrm{D}(\boldsymbol{\ell}_1+\boldsymbol{\ell}_2)\,P^{(i)}_\delta(\ell_1)\;, && \text{(A.5)}\end{aligned}$$

where $\overline{n}_\mathrm{sis} := N_\mathrm{h}/A_\mathrm{fov}$ expresses the mean number density of haloes. Therefore, we obtain in this scenario

$$P^{(i)}_\delta(\ell) = |\tilde{\delta}_\mathrm{sis}(\ell)|^2\overline{n}_\mathrm{sis}\;. \tag{A.6}$$